

Axion Dark Matter Experiment: Detailed design and operations

Cite as: Rev. Sci. Instrum. 92, 124502 (2021); doi: 10.1063/5.0037857

Submitted: 16 November 2020 • Accepted: 9 November 2021 •

Published Online: 9 December 2021



R. Khatiwada,^{1,a)} D. Bowring,² A. S. Chou,³ A. Sonnenschein,³ W. Wester,³ D. V. Mitchell,³ T. Braine,⁴ C. Bartram,⁴ R. Cervantes,⁴ N. Crisosto,⁴ N. Du,⁴ L. J. Rosenberg,⁴ G. Rybka,⁴ J. Yang,⁴ D. Will,⁴ S. Kimes,^{4,b)} G. Carosi,⁵ N. Woollett,⁵ S. Durham,⁵ L. D. Duffy,⁶ R. Bradley,⁷ C. Boutan,⁸ M. Jones,⁸ B. H. LaRoque,⁸ N. S. Oblath,⁸ M. S. Taubman,⁸ J. Tedeschi,⁸ John Clarke,⁹ A. Dove,⁹ A. Hashim,⁹ I. Siddiqi,⁹ N. Stevenson,⁹ A. Eddins,^{9,c)} S. R. O'Kelley,^{9,d)} S. Nawaz,^{9,e)} A. Agrawal,¹⁰ A. V. Dixit,¹⁰ J. R. Gleason,¹¹ S. Jois,¹¹ P. Sikivie,¹¹ N. S. Sullivan,¹¹ D. B. Tanner,¹¹ J. A. Solomon,^{11,f)} E. Lentz,¹² E. J. Daw,¹³ M. G. Perry,¹³ J. H. Buckley,¹⁴ P. M. Harrington,¹⁴ E. A. Henriksen,¹⁴ K. W. Murch,¹⁴ and G. C. Hilton¹⁵

AFFILIATIONS

¹ Department of Physics, Illinois Institute of Technology, Chicago, Illinois 60616, USA and Fermilab Quantum Institute, Fermi National Accelerator Laboratory, Batavia, Illinois 60510, USA

² Accelerator Physics Division, Fermi National Accelerator Laboratory, Batavia, Illinois 60510, USA

³ Particle Physics Division, Fermi National Accelerator Laboratory, Batavia, Illinois 60510, USA

⁴ Department of Physics, University of Washington, Seattle, Washington 98195, USA

⁵ Nuclear and Chemical Sciences Division, Lawrence Livermore National Laboratory, Livermore, California 94550, USA

⁶ Accelerators and Electrodynamics Group, Los Alamos National Laboratory, Los Alamos, New Mexico 87545, USA

⁷ NRAO Technology Center, National Radio Astronomy Observatory, Charlottesville, Virginia 22903, USA

⁸ National Security Directorate, Pacific Northwest National Laboratory, Richland, Washington 99354, USA

⁹ Department of Physics, University of California, Berkeley, California 94720, USA

¹⁰ Department of Physics, University of Chicago, Chicago, Illinois 60637, USA

¹¹ Department of Physics, University of Florida, Gainesville, Florida 32611, USA

¹² Department of Physics, University of Göttingen, 37073 Göttingen, Germany

¹³ Department of Physics, University of Sheffield, Sheffield S10 2TN, United Kingdom

¹⁴ Department of Physics, Washington University, St. Louis, Missouri 63130, USA

¹⁵ Physical Measurement Laboratory, National Institute of Standards and Technology, Gaithersburg, Maryland 20899, USA

^{a)} Author to whom correspondence should be addressed: rkhatiwada@iit.edu

^{b)} Current address: Microsoft Quantum, Microsoft, Redmond, WA 98052, USA.

^{c)} Current address: IBM Quantum, IBM Almaden Research Center, San Jose, CA 95120, USA.

^{d)} Current address: Physics division, Lawrence Livermore National Laboratory, Livermore, CA 94550, USA.

^{e)} Current address: Department of Manufacturing Engineering, Global Communication Semiconductors Inc., Torrance, CA 90505, USA.

^{f)} Current address: Department of Physics and Astronomy, University of North Carolina, Chapel Hill, NC 27599, USA.

ABSTRACT

Axion dark matter experiment ultra-low noise haloscope technology has enabled the successful completion of two science runs (1A and 1B) that looked for dark matter axions in the 2.66–3.1 μeV mass range with Dine–Fischler–Srednicki–Zhitnisky sensitivity [Du *et al.*, Phys. Rev. Lett. **120**, 151301 (2018) and Braine *et al.*, Phys. Rev. Lett. **124**, 101303 (2020)]. Therefore, it is the most sensitive axion search experiment to date in this mass range. We discuss the technological advances made in the last several years to achieve this sensitivity, which includes the implementation of components, such as the state-of-the-art quantum-noise-limited amplifiers and a dilution refrigerator. Furthermore, we

demonstrate the use of a frequency tunable microstrip superconducting quantum interference device amplifier in run 1A, and a Josephson parametric amplifier in run 1B, along with novel analysis tools that characterize the system noise temperature.

Published under an exclusive license by AIP Publishing. <https://doi.org/10.1063/5.0037857>

I. INTRODUCTION

Axions are hypothetical particles that exhibit characteristic behavior of dark matter; they are non-relativistic, highly stable, and weakly interacting.^{1–4} Axions were originally postulated to resolve the strong charge parity (CP) problem^{6,7} and would have been produced in the early universe through various mechanisms.^{2,3,8,9} Quantum chromodynamics (QCD) calculations suggest that axions could have a mass range of 1–100 μeV .^{10–12} The goal of achieving sensitivity to Grand Unified Theory (GUT)-scale Dine–Fischler–Srednicki–Zhitnisky (DFSZ) dark matter axions has motivated the Axion Dark Matter Experiment (ADMX) collaboration to implement new technologies in its recent axion searches with the primary focus on minimizing both the amplifier and cavity blackbody noises. As such, we implemented two critical pieces of technology in the ADMX haloscope: the state-of-the-art quantum amplifiers and a dilution refrigerator. While these were broadly the most notable technological improvements, the details varied between the runs and will be described below.

In run 1A, ADMX acquired data over an axion mass range from 2.66 to 2.81 μeV from January to June 2017, demonstrating the sustained use of a Microstrip Superconducting Quantum Interference Device (SQUID) Amplifier (MSA) in the frequency range of 645–680 MHz. This was followed by the implementation of a Josephson Parametric Amplifier (JPA) in run 1B (January–October 2018), covering 680–790 MHz, corresponding to an axion mass range of 2.81–3.31 μeV . Both sets of quantum amplifiers combined with the order of magnitude reduction in physical temperature have dramatically improved ADMX performance over previous operations.¹² We have refined techniques for measuring the reduced system noise temperature and have incorporated it into the analysis. The implementation of a model JDR-800³He/⁴He dilution refrigerator system to cool the cavity enabled us to minimize the thermal noise for both runs. In run 1A, this led to an average cavity temperature of about 150 mK, whereas in run 1B, we achieved an average cavity temperature of about 130 mK. In addition, we discuss a few other advances to improve our sensitivity. These include a complete update of the Data Acquisition System (DAQ) software and the implementation of hardware for the blind injection of synthetic axion signals. Meanwhile, ADMX has expanded the search to higher mass as a part of ongoing research and development efforts. The prototype “Sidecar” cavity system attained new mass limits in three distinct frequency regions around 4.2, 5.4, and 7.2 GHz.¹³ We briefly discuss instrumentation advancements for Sidecar because it shares the detector volume with the ADMX.

II. ADMX OVERVIEW

The existence of axions would modify Maxwell’s equations as follows:

$$\vec{\nabla} \cdot \vec{E} = \rho - g_{a\gamma\gamma} \vec{B} \cdot \vec{\nabla} a, \quad (1)$$

$$\vec{\nabla} \cdot \vec{B} = 0, \quad (2)$$

$$\vec{\nabla} \times \vec{E} = -\frac{\partial \vec{B}}{\partial t}, \quad (3)$$

$$\vec{\nabla} \times \vec{B} = \frac{\partial \vec{E}}{\partial t} + \vec{J} - g_{a\gamma\gamma} \left(\vec{E} \times \vec{\nabla} a - \frac{\partial a}{\partial t} \vec{B} \right). \quad (4)$$

Here, \vec{E} and \vec{B} are the electric and magnetic fields, $c = \frac{1}{\sqrt{\epsilon_0 \mu_0}} = 1$, ρ is the charge density, \vec{J} is the source current, a is the scalar axion field, and $g_{a\gamma\gamma}$ is the axion-two-photon coupling constant, which is related to the model-dependent axion-to-photon coupling constant g_γ by $g_{a\gamma\gamma} = \alpha g_\gamma / \pi (f_{PQ}/N)$,^{15,16} where α is the fine structure constant, f_{PQ} is the Peccei Quinn symmetry breaking scale, and N is the number of quark flavors.

The two primary models for the axion-to-photon coupling are known as KSVZ (Kim–Shifman–Vainshtein–Zakharov)^{17,18} and DFSZ (Dine–Fischler–Srednicki–Zhitnisky).^{19,20} KSVZ couples only to hadrons, whereas DFSZ couples to both hadrons and leptons. These couplings (g_γ) have values of -0.97 and 0.36 , respectively. DFSZ couplings are about a factor of 3 weaker than KSVZ couplings and so require greater experimental effort to detect. Therefore, reaching the DFSZ sensitivity has been long sought after the goal of axion experiments. The application of the magnetic field provides a new channel for axions to decay into a photon, whose frequency is given by $f = E/h$, where E corresponds to the total energy of the axion with contributions primarily from the rest mass energy and a small kinetic energy term and “ h ” is Planck’s constant. This is known as the inverse Primakoff effect. The conversion is expressed by using a Feynman diagram in Fig. 1.

In 1983, Sikivie introduced the axion haloscope, which uses a large density of virtual photons from a strong static magnetic field to allow the galactic axions to convert into real photons inside a microwave cavity. When the axion’s frequency matches the resonance frequency of the microwave cavity, the conversion rate is enhanced to detectable levels. The power deposited in the cavity due to this conversion is given by²⁰

$$P_{a \rightarrow \gamma\gamma} = (1.9 \times 10^{-22} \text{ W}) \left(\frac{V}{136 \text{ l}} \right) \left(\frac{B}{6.8 \text{ T}} \right)^2 \times \left(\frac{C_{nlm}}{0.4} \right) \left(\frac{g_\gamma}{0.97} \right)^2 \left(\frac{\rho_a}{0.45 \text{ GeV/cm}^3} \right) \times \left(\frac{f_a}{650 \text{ MHz}} \right) \left(\frac{Q}{50\,000} \right). \quad (5)$$

Here, V is the volume of the cavity, B is the magnetic field, C_{nlm} is the form factor of the cavity, ρ_a is the local dark matter density, f_a is the frequency of the photon, and Q is the loaded quality factor

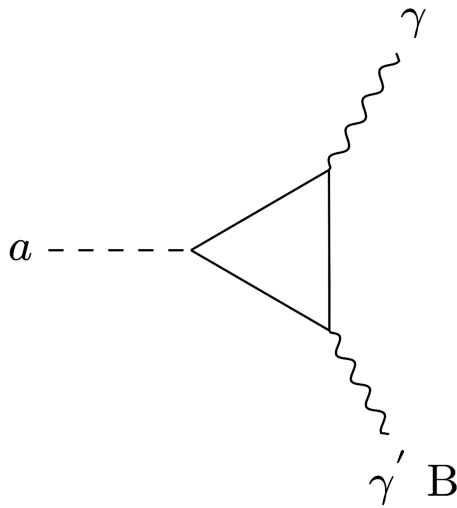


FIG. 1. Feynman diagram of the inverse Primakoff effect. An axion a converts into a photon γ by interacting with a virtual photon γ' in a static magnetic field B through the fermionic loop. The coupling constant is denoted by $g_{a\gamma\gamma}$.

of the cavity. The form factor is defined as the integral of the overlap between the electric field of the cavity transverse magnetic (TM) mode and the external magnetic field generated by the magnet.²⁰ For any given mode in an empty cylindrical cavity, the TM_{010} mode has the highest form factor and the cavity radial dimension corresponds to approximately one-half of the photon wavelength. In practice, the geometry of the cavity is more complicated because of the presence of tuning rods, so simulation is necessary to understand the form factor.

From Eq. (5), it is clear that experimentalists have several handles, which can be used to optimize the power extracted by the receiver. The cavity volume, magnetic field, and quality factor can all be maximized, whereas the remaining parameters (g_γ and ρ_a) are fixed by nature. The signal-to-noise ratio (SNR) is defined by the following Dicke radiometer equation:²¹

$$\frac{S}{N} = \frac{P_{a \rightarrow \gamma\gamma}}{k_B T_{sys}} \sqrt{\frac{t}{b}}. \quad (6)$$

Here, S is the signal, N is the noise, $P_{a \rightarrow \gamma\gamma}$ is the power that would be deposited in the cavity in the event of an axion signal, k_B is the Boltzmann constant, T_{sys} is the system noise temperature, t is the integration time, and b is the measurement frequency bandwidth. The total system noise temperature T_{sys} is composed of cavity blackbody noise and amplifier noise, which should be minimized to achieve the highest possible SNR.

III. THE DETECTOR

ADMX is located at the Center for Experimental Nuclear Physics and Astrophysics (CENPA) at the University of Washington, Seattle. The ADMX detector consists of several components collectively referred to as “the insert,” shown in Fig. 2. The insert is lowered into the bore of a superconducting solenoid magnet, which is operated typically at just under 8 T, for data-taking operations.

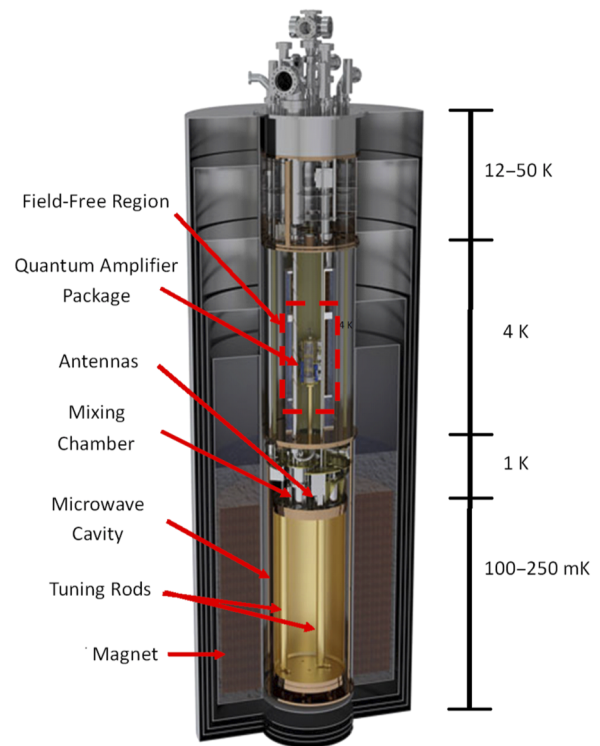


FIG. 2. Schematic of ADMX detector components. The microwave cavity can be seen at the center with tuning rods. The central cylindrical structure containing the cavity and electronics that is inserted into the magnet bore is called “the insert.” Various temperature stages are indicated on the right-hand side. The quantum amplifier package is thermalized to the microwave cavity.

The cylindrical insert (0.59 m diameter and 3 m height) contains the microwave cavity, motion control system for the antenna and cavity tuning rods, cryogenic and quantum electronics, a dilution refrigerator, a liquid ^4He reservoir, a bucking magnet, and the Sidecar cavity and electronics. The insert is designed such that the field sensitive quantum amplifiers, switches, and circulators are housed in a field-free region, with a volume 0.22 m height by 0.15 m diameter, provided by a bucking coil. The cavity is inserted concentrically in the magnet bore to maximize the form factor. The insert also involves a Cryomech PT60 pulse tube cooler that cools the top of the insert to 50 K. Below that, a liquid ^4He reservoir maintains the bucking coil and second-stage High Electron Mobility Transistor (HEMT) amplifiers near 4 K. Two pumped ^4He refrigerators were used: one is thermally tied to the motion control system and the thermal shields surrounding the cavity and counters the thermal load of moving tuning rods and the other pre-cools the $^3\text{He}/^4\text{He}$ mixture used in the dilution refrigerator before it enters the still chamber. The dilution refrigerator mixing chamber is thermally anchored to both the first-stage cryogenic electronics and the microwave cavity.

A. Magnets

ADMX operated a superconducting magnet²² at 6.8 and 7.6 T, respectively, for runs 1A and 1B. The magnet requires ~ 2000 l of

liquid helium per month for continuous cooling during data-taking operations (supplied by a closed loop Linde liquefier system). The cavity is concentrically located inside the magnet such that the cavity axis aligns with the applied magnetic field direction. The bucking magnet¹² reduces the magnetic field at the site of the electronics package to below 0.1 mT by canceling any external stray magnetic field from the main magnet. Two Hall probes are located on each end of the bucking coil to monitor the field at the electronics site during data acquisition to ensure that it is within tolerable limits. The Hall probes are both model HGCT-3020 InAs Hall generators from Lakeshore.

B. Cavity

The ADMX cavity is a copper-plated stainless steel (136 l) right-circular cylindrical cavity ~ 1 m in length and 0.4 m in diameter. Two 0.05 m diameter copper tuning rods run through the length of the cavity and are moved translationally from the walls to near the center using aluminum-oxide rotary armatures. This allows the fundamental TM_{010} -like mode that couples to the detector to be

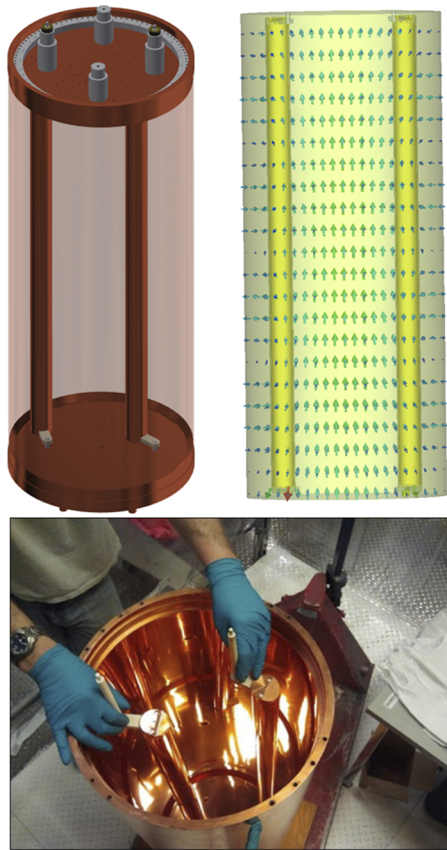


FIG. 3. ADMX cavity system. The top left panel shows a cutaway view of the CAD model. The top right panel represents a computer simulation technology (Dassault Systèmes) microwave studio simulation²⁴ of the TM_{010} mode with each of the rods at 116° from the center. The bottom panel represents a picture of the system with the top end cap removed showing two 0.05 m diameter tuning rods and their aluminum-oxide ceramic axles.

varied from 580 to 890 MHz. Both the stainless steel cavity and the copper tuning rods are plated with oxygen-free high thermal conductivity (OFHC) copper to a minimum thickness of 0.08 mm and then annealed for 8 h at 400°C in vacuum. The annealing process increases the grain-size of the copper crystals, leading to longer electron scattering path lengths as the copper is cooled into the anomalous skin depth regime and thus producing high Q-factors for the detector.²³ The cavity system and the magnetic field profile of the main magnet can be seen in Figs. 3 and 4.

The quality factor of the cavity modes is frequency dependent and is measured periodically via a transmission measurement made through the weakly coupled port to the output port. The presence of the tuning rod lowers the quality factor of an empty cavity. A quality factor between 30 000 and 50 000 was typically achieved in runs 1A and 1B with the average around 40 000. During mode-crossings when the Transverse Magnetic (TM) modes mix with a static Transverse Electric (TE) or Transverse Electromagnetic (TEM) modes, the fitting functions return anomalously high Q-factors (80k or above). Such frequency regions were excluded from the dataset. The form factor for the cavity is calculated from simulation. The mode structure of the simulation is compared to that measured from the cavity to ensure accuracy. The resulting E-field is convolved with a model of the B-field produced by the magnet. The form factor of the TM_{010} varies with frequency and rod position with an average value of 0.4.

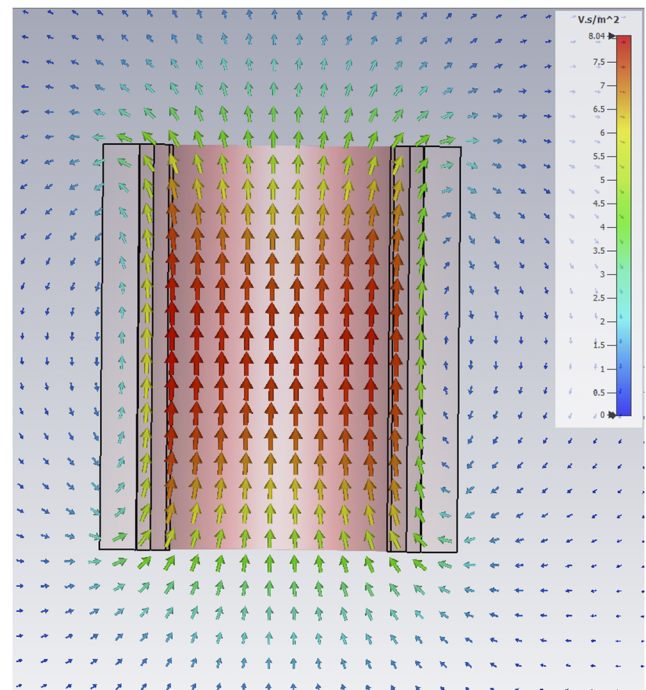


FIG. 4. ADMX magnet system simulated using the computer simulation technology (Dassault Systèmes) magnetic field solver.²⁴ This shows the magnet field profile with the maximum (8 T) at the center. This field profile was used to convolve the form factor for the resonant mode in Fig. 3.

C. Mechanical/motion control system

Two copper-plated tuning rods swept out the 0.09 m radius circular trajectories shown in Fig. 5. They are rotated from the walls of the cavity ($\theta = 0$), where they minimally impact the electromagnetic boundary conditions of the resonator, to the center where the TM_{010} frequency is at its highest ($\theta = 180$). The armatures that protrude through the end caps and offset the rods are made of alumina. This prevents the rods from acting as antennas and thus radiating power out of the system. Mechanical motion is translated to the rods via room temperature stepper motors mounted on the top plate of the insert. Acting through vacuum feedthroughs, these stepper motors communicate motion to long G10 fiberglass shafts that connect to gear boxes (see the upper left panel of Fig. 5). The gear boxes have minimal backlash (a 19 600 : 1 gear reduction), allowing for micro-radian positioning of the tuning rods. A variable depth antenna located on the top of the cavity picks up an axion signal from the cavity and transmits it to the amplifiers. This semi-rigid and coaxial antenna attaches to a different gear box, which turns rotary motion

from the room temperature stepper motor into linear depth control. The depth of the antenna is adjusted to maintain a critical coupling to the TM_{010} mode. When it is critically coupled (or impedance matched) to the cavity on resonance, the power escaping through the antenna equals the power lost in the walls of the cavity, whereas off-resonance most of the power is reflected. The coupling is determined by reflecting swept power from the cavity and measuring its magnitude. This was achieved with the network analyzer and a circulator shown in Fig. 6. The swept output of the network analyzer is directed by using the circulator toward the cavity. Power reflected from the cavity then travels back to the circulator, up the receiver chain, and back to the input of the network analyzer. A good impedance match is marked by a deep trough in the reflected baseline on resonance. The depth of the antenna is adjusted to minimize the depth of this trough. Conventionally, when the difference between the minima of the trough and the off-resonance baseline reaches -30 dB, the antenna is considered critically coupled. This means that only 0.1% of the on resonance incident power is reflected.

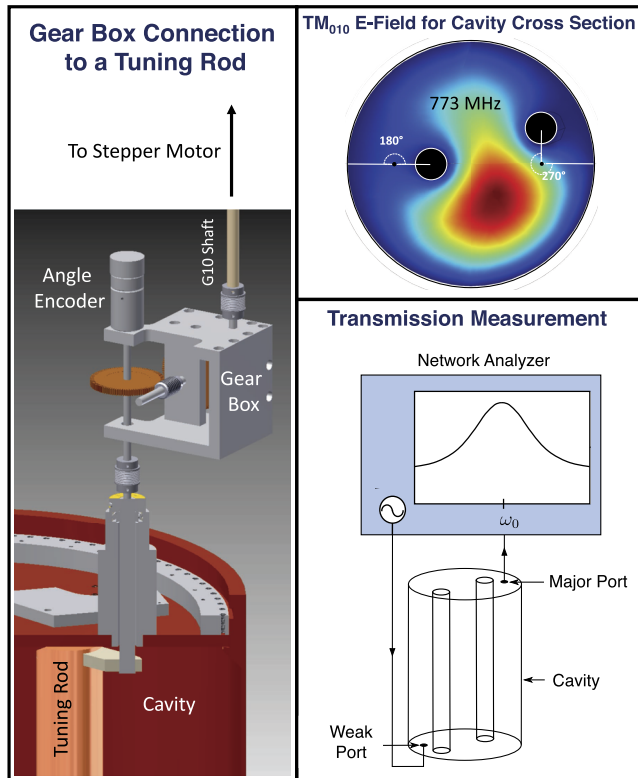


FIG. 5. Tuning mechanism of the main cavity,²⁵ reprinted with permission from C. Boutan, "A piezoelectrically tuned RF-cavity search for dark matter axions," Ph.D. thesis, University of Washington, 2017. Left: a room temperature stepper motor rotates a G10 fiberglass shaft connected to a gear box. This motion undergoes a 1 : 19 600 gear reduction and rotates the tuning rod in the cavity. Top right: rotation of the tuning rods changes the boundary conditions in the cavity and alters the resonant frequency. Bottom right: the resonant frequency of the cavity is determined by injecting swept power from a network analyzer into a weakly coupled antenna. The swept power is picked up by using the critically coupled antenna to measure the transfer function of the cavity.

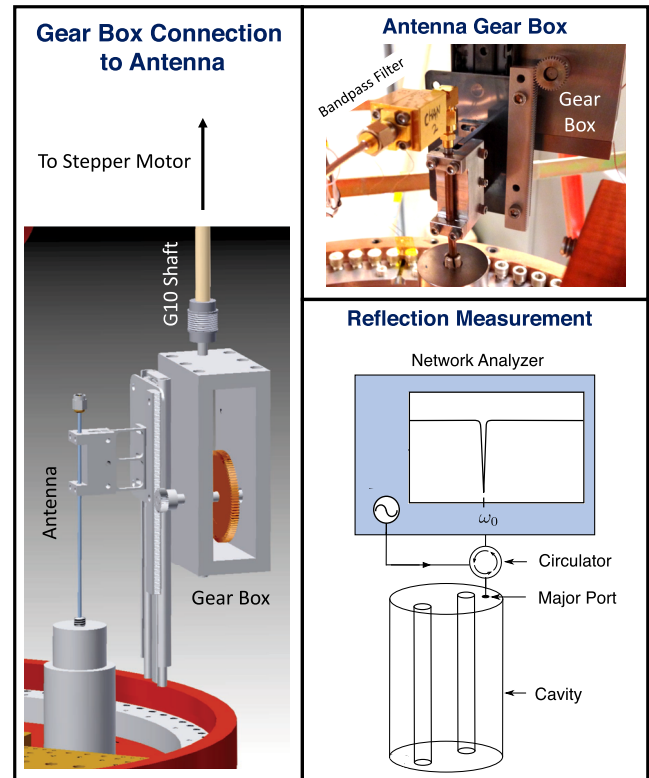


FIG. 6. Antenna coupling mechanism for the main experiment,²⁵ reprinted with permission from C. Boutan, "A piezoelectrically tuned RF-cavity search for dark matter axions," Ph.D. thesis, University of Washington, 2017. Left: a room temperature stepper motor rotates a G10 fiberglass shaft connected to a gear box. Rotary motion is converted to linear motion, which inserts or removes the antenna from the cavity. Top right: an image of the linear gear box holding the coaxial antenna. Bottom right: the antenna coupling is determined by reflecting swept power from a network analyzer off of the antenna. If the antenna is critically coupled, maximum incident power on resonance will be absorbed into the cavity, as indicated by a deep trough in the reflection measurement.

D. Cryogenic electronics package

The main body of the cryogenic electronic package system sits inside the field-free region (Fig. 2) and contains the most delicate part of the experiment, the cryogenic radiofrequency (RF) electronics, and quantum amplifier package. This includes quantum-noise-limited amplifiers [Berkeley (University of California Berkeley)], circulators (run 1A: Quinstar UTB1262KCS and run 1B: QCY-007020UM00), directional couplers (Pasternack), switches (Radiall R585433210), and a dc block for run 1A. The OFHC copper frame houses these electronics in the cryogenic electronic package. Figure 7 shows an example of the cryogenic electronic package. Since most of the RF electronics are frequency dependent, they are swapped for different runs according to the target frequency range corresponding to different axion masses.

Physical and amplifier noise temperatures of the cryogenic electronics housed in the package determine the total noise temperature of the system. Thus, keeping the cryogenic electronic package thermalized to the dilution refrigerator and characterizing the electronics are extremely important in determining the sensitivity of the experiment. For run 1A (1B), the cryogenic electronic package was at a physical temperature of 300 (230 mK) despite being heat sunk to the cavity, which was at 150 (130 mK). A newly designed cryogenic electronics package for run 1C incorporated better thermalization of the various electronics into its frame and also into the dilution refrigerator and removed the thermal short caused by misalignment to the liquid ^4He reservoir. As a result, this design reduced the physical temperature of the electronics and components to 120 mK (with a mixing chamber temperature of 100 mK) in 2020 during run 1C. In the following paragraphs, differences between runs 1A and 1B of the cryogenic electronics package circuitry will be discussed.

The cryogenic electronics package initially housed two separate antennas extracting power from the cavity: the first coupled to the main cavity TM_{010} mode and the second coupled to the TM_{020} mode. In addition, a third antenna coupled to the Sidecar TM_{010} or TM_{020} mode. The TM_{020} main cavity antenna was not used since its HEMT amplifier failed to operate early into run 1A and was removed in the subsequent runs.

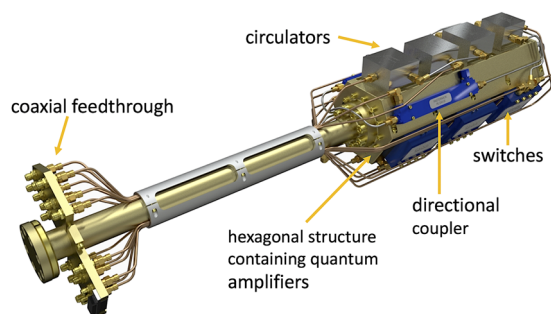


FIG. 7. Latest cryogenic electronics package design with the electronics and accessories being used in run 1C (2020). The quantum electronics are housed inside the hexagonal chamber in a mu-metal shield. The hexagonal part is located in a zero magnetic field region of the ADMX detector to avoid damage to the delicate quantum electronics. The antenna goes to the cavity and higher temperature electronics, such as HEMT through the feedthrough flange shown at the bottom of the cryogenic electronics package shaft.

Figure 8 shows the schematic of the antenna used for data-taking in run 1A (discussed in Ref. 26). Similarly, Fig. 9 shows the main cavity TM_{010} antenna used to take data in run 1B (published in Ref. 27). Any photon signal generated by axions deposited in the cavity passes through the output chain electronics containing a series of switches and circulators to the first-stage quantum amplifiers and further to the HEMT (Low Noise Factory, run 1A: LNC03_14A, run 1B: LNF-LNC0.6_2A) with an additional series of room temperature amplifiers (Minicircuits) before being digitized (Signatech). The cryogenic electronics package was wired with copper coaxial cables (Pasternack), whereas the cavity antenna was made from semi-rigid 0.0022 m diameter NbTi superconducting coax (Keycom NbTiNbTi085) with ~ 0.025 m of the center conductor exposed. NbTi provided a thermal disconnect from the 100 mK cavity to the 1 K linear drive that the antennas were attached to. Flexible coaxial lines were used to connect to the cryogenic electronics package inputs, which were coupled to the first-stage quantum amplifiers via NbTi cables in the RF output chain. Coaxial cables in the input chain were stainless steel (Keycom ULT-03).

Any photon signals emerging from the cooled cavity are amplified by using quantum amplifiers: the MSA (run 1A) and JPA (run 1B). The building block of modern quantum amplifiers, the DC SQUID, will be discussed in Sec. III D 1. Furthermore, both the MSA and the JPA were fabricated by Berkeley specifically for the ADMX frequency range and their fabrication and properties will be discussed in detail below.

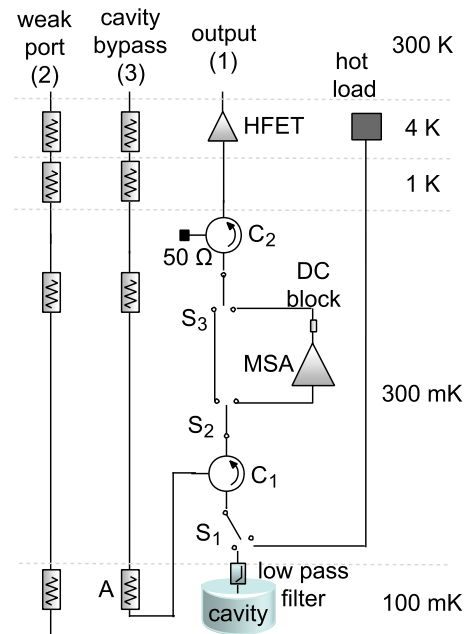


FIG. 8. Insert schematic of the run 1A antenna. It consisted of attenuators in the input lines, circulators (C_1 and C_2), a low-pass filter, a switch (S_1), a MSA, a dc block, a variable resistor (hot load), and a HEMT amplifier connected to the cavity through coaxial cable. The switch enables the characterization of the system noise by switching to the heated “hot load” from the cavity.

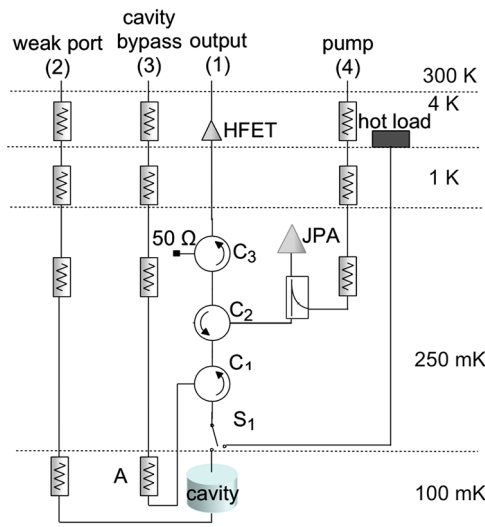


FIG. 9. Insert schematic of the run 1B antenna. Reprinted with permission from Bartram *et al.*, Phys. Rev. D **103**, 032002 (2021). Copyright 2021 American Physical Society. It consisted of attenuators in the input lines, circulators (C_1 , C_2 , and C_3), a switch S_1 , a directional coupler, a JPA, a variable resistor (hot load), and a HEMT amplifier connected to the cavity through coaxial cable. The switch enables characterization of the system noise by switching from the cavity to the “hot load.”

1. DC SQUID

The building block of quantum amplifiers consists of a conventional dc Superconducting Quantum Interference Device (SQUID),^{29–31} shown schematically in Fig. 10(a), with an integrated, tuned RF input coil. Since the SQUID is operated in the voltage state, the Stewart–McCumber parameter^{32,33} $\beta_c \equiv 2\pi R^2 I_0 C / \Phi_0$ must be less than unity to ensure a non-hysteretic current–voltage (I – V) characteristic. Here, R is the Josephson junction³³ shunt resistance, I_0 is the junction critical current, C is the intrinsic junction capacitance, and $\Phi_0 \equiv h/2e \approx 2.07 \times 10^{-15}$ T m² is the flux quantum, where h is Planck’s constant and e is the electronic charge. The lowest noise energy of the SQUID, $S_\Phi(f)/2L$, is obtained when reduced SQUID inductance $\beta_L \equiv 2LI_0/\Phi_0 = 1$ and β_c is at a value just below the onset of hysteresis;³⁰ here, L is the geometric loop inductance and $S_\Phi(f)$ is the spectral density of the flux noise. Figure 10(b) shows a typical

I – V characteristic for the SQUID, biased with a constant current, illustrating the change in critical current and observed change in output voltage for applied flux, $\Phi_a = n\Phi_0$ and $(n + 1/2)\Phi_0$. In typical amplifier operation, the flux bias is set close to $(n \pm 1/4)\Phi_0$ to maximize the flux-to-voltage transfer coefficient $V_\Phi \equiv \partial V / \partial \Phi_a$, as illustrated in Fig. 10(c).

The layout of a typical SQUID, fabricated from photolithography patterned thin superconducting films, is shown schematically in Fig. 11(a).³⁴ The superconducting loop is deposited as a square washer interrupted by a narrow gap. The gap is bridged by a second superconducting layer, the “counterelectrode” connecting to each side of the gap via a Josephson junction. The input coil is deposited on top of an electrically insulating film overlaying the SQUID washer so that current in the input coil efficiently couples flux to the SQUID loop. Figure 11(b) shows a SQUID with an 11-turn input coil. By coupling the input loop to an appropriate input circuit, one can realize a highly sensitive amplifier.

2. Microstrip SQUID Amplifier (MSA): Principles and fabrication

With a conventional flux coupling between the input coil and the SQUID, the highest practical operating frequency of such amplifiers is limited to a few 100 MHz. This is because with increasing frequency, the parasitic capacitance between the input coil and the SQUID washer conducts a larger fraction of the input signal as a displacement current, reducing the magnetic flux coupled into the SQUID. This limitation is eliminated with the Microstrip SQUID Amplifier (MSA),^{36–38} which makes the washer-coil capacitance an integral component of a resonant microstrip input. The MSA was invented specifically to meet the needs of ADMX by John Clarke’s group at Berkeley. The circuit configuration of the MSA is shown schematically in Fig. 12. The microstrip is represented as a distributed inductance and capacitance between the input coil and the SQUID washer.^{36,37}

The spiral input microstrip behaves as a $\lambda/2$ resonator of length ℓ when its termination is open, provided that the coupling to the input line is weak, for instance, due to an impedance mismatch and large coupling capacitor reactance. One tunes the MSA by terminating the microstrip with a voltage-controlled capacitor (varactor diode), enabling one to change the electrical length of the microstrip without changing the characteristic impedance Z_0 . A detailed account of MSA gain, noise, and resonant frequency appears

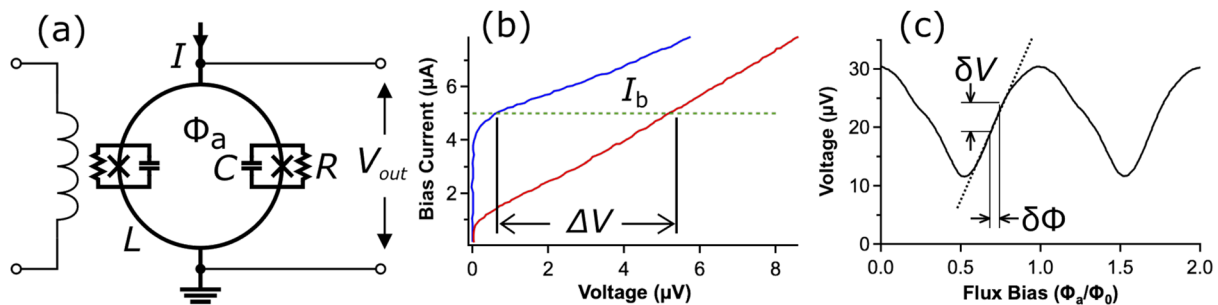


FIG. 10. DC SQUID. (a) Schematic, with Josephson junctions indicated with “X.” (b) Voltage V vs current I for the applied magnetic flux $\Phi_a = n\Phi_0$ and $(n + 1/2)\Phi_0$. Voltage change ΔV at a constant bias current I_b . (c) Voltage V vs normalized magnetic flux Φ_a/Φ_0 at constant I_b .

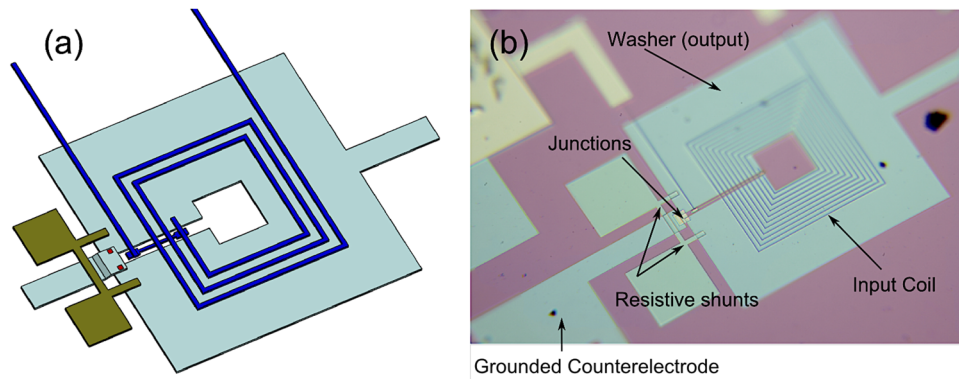


FIG. 11. Microstrip SQUID Amplifier (MSA). (a) Simplified schematic diagram (not to scale). The small red squares represent Josephson junctions. (b) Optical photograph of 11-turn MSA. Microstrip leads enter from the top. Junctions and resistors are at the lower-left edge.

in Ref. 36. At low temperatures, the MSA can achieve quantum limited amplification.³⁸

Fabrication of the MSA largely follows the standard process³⁹ at the National Institute of Science and Technology, Boulder. This process utilizes an *in situ* sputtered trilayer of Nb, Al, and Nb for the Josephson junction, e-beam evaporated PdAu shunt resistors, a plasma-enhanced chemical vapor deposited SiO₂ dielectric, and an additional sputtered Nb wiring layer. The detailed discussion of MSA principles and fabrication can be found in Ref. 40.

3. The Microstrip SQUID Amplifier (MSA): Operation and tuning

Figure 13 shows the MSA mounted on its RF carrier board. The signal from the cavity is transmitted to the MSA via a 50-Ω coaxial transmission line to the RF board, followed by a 50-Ω coplanar waveguide and a fixed capacitor sized for optimal coupling to the resonant microstrip. When the ADMX cavity frequency is changed by positioning tuning rods, the MSA resonant frequency is tuned

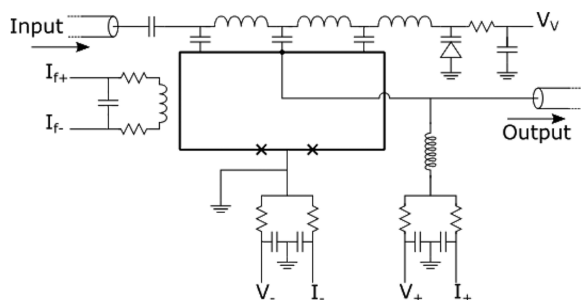


FIG. 12. Schematic diagram of the MSA with the grounded counter electrode. The signal enters from left through the coupling capacitor to the input coil, represented as a distributed inductance and capacitance to the SQUID loop. End of the input coil is terminated by a varactor diode to ground at top right. DC varactor bias voltage V_V determines varactor capacitance and input coil resonant frequency. Bias current I_0 greater than I_c applied from I_+ to I_- maintains SQUID in the voltage state. The terminals V_+ and V_- are for diagnostic purposes, not essential for operation. The inductor at left couples static flux to the SQUID to set $\Phi_a \approx (n \pm 1/4)\Phi_0$ to maximize the transfer coefficient $\partial V / \partial \Phi_a$. SQUID output voltage is connected via a 50-Ω line to a transistor-based amplifier.

by applying a dc bias to the terminating varactor. A $\lambda/2$ resonance assumes an open circuit (π reflection) at both ends, but if either end of the MSA input coil is not an open circuit, the $\lambda/2$ resonant frequency ω_0 is altered by $\omega = \omega_0(\phi_{in} + \phi_{end})/2\pi$, where the reflected phases ϕ_x are given by $\tan(\phi_x/2) = iZ_x/Z_0$. Here, Z_x is the loading impedance at either end of the microstrip and Z_0 is the input coil ac impedance.⁴⁰ This formula is general—purely reactive loads generate a real reflected phase, but a real (resistive) load component generates an imaginary (lossy) reflected phase. The varactors⁴¹ appear at the top-right corner of the schematic in Fig. 12 and at the lower-left corner of the MSA in Fig. 13. All dc bias signals (current, flux, and varactor tuning) pass through discrete RC low-pass filters mounted on the RF carrier.

It is challenging to achieve substantial gain with a conventional MSA at frequencies above 1 GHz. Subsequent development of the MSA, however, in which it is operated in higher order modes than the $\lambda/2$ mode, enables high gain at gigahertz frequencies, for example, 24 dB at 2.6 GHz.⁴²

Figure 14 shows the gain vs frequency of the MSA as measured at Berkeley (UCB) and at Seattle (UW). The difference in performance is stark. We note that at UCB, the MSA was connected to ideal 50-Ω loads, required magnetic shielding only from the ambient 50-μT geomagnetic field, and was operated at a bath temperature

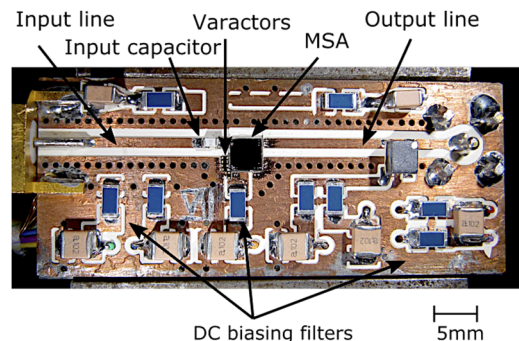


FIG. 13. Photograph of a MSA.

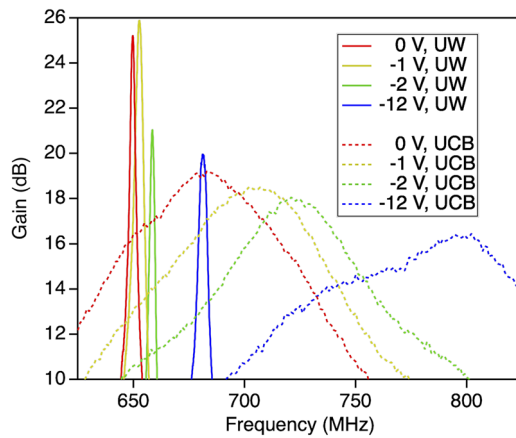


FIG. 14. MSA tuning vs varactor voltage bias from 0 to -12 V. On the Y axis is the MSA gain in dB. The dashed lines denote UCB data, and the solid lines denote data from UW run 1A.

of 60 mK. At UW, the MSA was connected to switches and circulators that may have non-negligible S_{11} parameters. Furthermore, it required both active cancellation and passive cancellation of the 6.8 T haloscope magnetic field and was operated at a bath temperature of 300 mK. Despite the unexpected performance, the noise temperature was sufficiently low to achieve sensitivity to the DFSZ threshold (see Sec. V D 4).

In the transition from run 1A to run 1B, ADMX switched from MSA to JPA technology.

4. Josephson Parametric Amplifier (JPA): Device and operation

The JPA is a low noise microwave amplifier based on the Josephson junction.³³ JPAs have been developed to achieve quantum limited amplification,⁴³ adding only a minimum amount of noise required by quantum mechanics.⁴⁴ JPAs used by ADMX were fabricated at Berkeley by Siddiqi's group. A typical JPA can achieve 20+ dB of power gain over an instantaneous bandwidth of 10–20 MHz.

The JPA is a non-linear oscillator that consists of a SQUID loop^{29,30} or an array of SQUID loops shunted by a geometric capacitance, as shown in Fig. 15. The resonant frequency of a JPA is given by $\omega_0 = 1/\sqrt{(L_J + L_G)C}$, where L_J is the total Josephson inductance of the SQUID loop, C is the shunting capacitance, and L_G is the geometric or stray inductance in the circuit. The inductance of a single Josephson junction can be expressed as

$$L_J = \frac{L_{J0}}{\sqrt{1 - (I/I_0)^2}} = L_{J0} \left(1 + \frac{1}{2} (I/I_0)^2 + \dots \right), \quad (7)$$

where I_0 is the critical current of the junction, $L_{J0} = \Phi_0/2\pi I_0$ is the Josephson inductance in the absence of any supercurrent flow I through the junction, and Φ_0 is the flux quantum. The non-linearity of the junction inductance can be understood through the series expansion of L_J , which, for $I \ll I_0$, can be truncated at the quadratic term. The behavior of two Josephson junctions in a SQUID loop can be modeled as a single Josephson junction but with a flux-tunable critical current. The critical current I_c of a SQUID can be expressed as a function of an externally applied magnetic flux Φ_E ,

$$I_c(\Phi_E) = 2I_0 \left| \cos \left(\frac{\pi \Phi_E}{\Phi_0} \right) \right|, \quad (8)$$

where I_0 is taken to be identical for both Josephson junctions. Since L_J is a function of the critical current I_c and I_c increases non-linearly with an external flux bias through the loop (until the field enclosed is equal to half a flux quantum), the resonant frequency of the device can be tuned downward from its zero-bias state, as shown in Fig. 16.

The operation of a JPA can be understood using the classical picture of parametric amplification: a strong pump tone at ω_p transfers energy to the weak signal at ω_0 generating more photons at ω_0 by conservation of energy. A JPA can be operated as a phase-preserving or phase-sensitive amplifier. In phase-preserving amplification, the phase difference between the pump tone and the signal tone is random, leading to an amplification of both quadratures of the readout signal by a factor of \sqrt{G} , where G is the power gain of the JPA. Phase-preserving amplification adds at least half a photon of noise to the readout signal,⁴⁵ as required by quantum mechanics. In phase-sensitive amplification, the pump tone is in phase with one of the

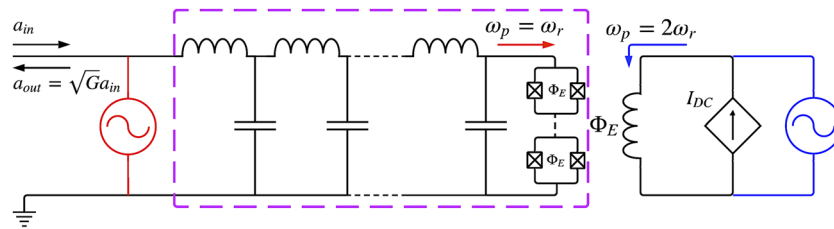


FIG. 15. The circuit diagram of a JPA consists of an array of SQUIDs in series with a geometric inductance and shunted by a capacitor (outlined in purple). When the capacitance and inductance are lumped elements in the transmission line leading to the SQUIDs, such as in coplanar waveguides, then it is typically called a lumped-JPA or LJPA. An external DC magnetic field is inductively coupled to the SQUIDs for flux tuning the resonant frequency. When flux-pumping a JPA at frequency $\omega_p = 2\omega_r$ (blue), where ω_r is the resonant frequency of the JPA, the pump tone is inductively coupled to the SQUIDs through an external coil or transmission line. When current-pumping a JPA at frequency $\omega_p = \omega_r$ (red), the pump tone propagates down the main transmission line. In both cases, the input signal a_{in} enters through the main transmission line, mixes with the pump tone in the JPA, and then is reflected back down the transmission line. For phase-preserving amplification, such as is done in the ADMX, the outgoing signal has been amplified by a factor \sqrt{G} with respect to the input signal, where G is the power gain of the JPA.

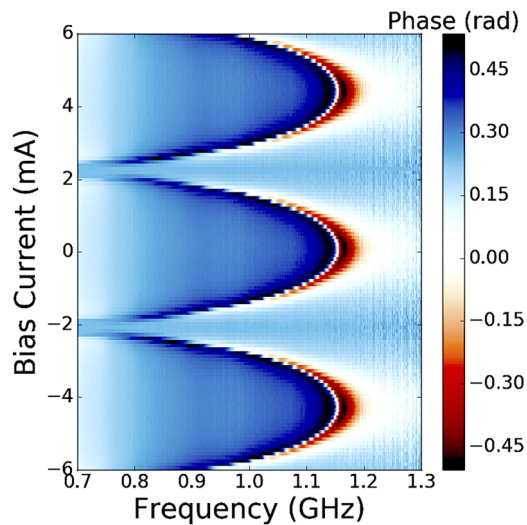


FIG. 16. A typical tuning curve produced for characterizing a JPA, demonstrating that the resonant frequency can be tuned downward from its zero-bias state. Each horizontal line is a single trace on a VNA for a given DC bias current. The resonant frequency is measured as a sharp phase shift in the phase of the reflected signal.

signal quadratures, leading to an amplification of $2\sqrt{G}$ for the in-phase quadrature and a de-amplification by the same factor for the out-of-phase quadrature. The JPA used in run 1B was operated in the phase-preserving mode for the duration of data-taking.

Depending on how the JPA is designed and operated, two different types of wave-mixing processes can occur. In the “current-pump” design,^{47–50} as shown in Fig. 17, both the signal tone and the pump tone enter the JPA through the main RF transmission line. In

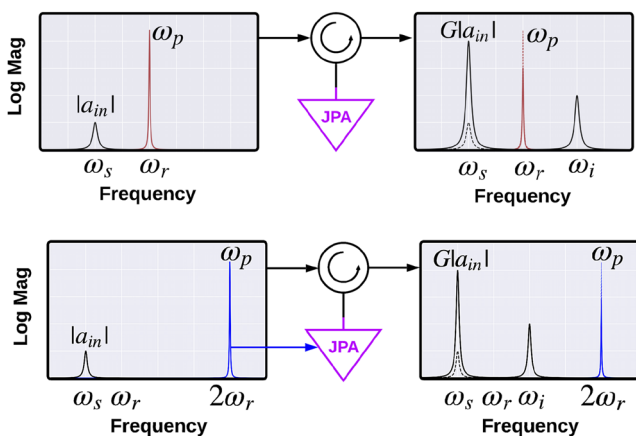


FIG. 17. Top: Current-pumping a JPA. In current-pumped JPAs, the small signal tone and strong pump tone both enter the JPA through the main transmission line. The output spectra contain the amplified signal, the depleted pump tone, and an idler signal. Bottom: Flux-pumping a JPA. In flux-pumped JPAs, the small signal tone enters the JPA through the main transmission line, but the strong pump tone is introduced through an external line inductively coupled to the SQUIDs. The output spectra contain the amplified signal, the depleted pump tone, and an idler signal.

this design, parametric amplification is achieved by modulating the current through the Josephson junctions in the SQUID at the resonant frequency of the device. Since the non-linearity of the device in this scheme is due to a fourth-order Kerr non-linearity,⁵⁰ the pump tone is not equal to twice the signal tone, but rather the two are approximately equal to each other, with only a slight detuning on the order of tens of MHz. This process results in four-wave mixing, in which two pump photons are converted into one signal photon and one idler photon. Energy conservation gives $2\omega_p = \omega_s + \omega_i$. The JPA used in the ADMX for run 1B was of the current-pump design.

In the “flux-pump” design,^{52–55} as shown in Fig. 17, the signal tone enters the JPA through the main RF transmission line, but the pump tone is inductively coupled to the SQUID. Thus, parametric amplification occurs by modulating the frequency of the resonator by means of an additional external AC magnetic flux. This design results in a three-wave mixing process, in which a single pump photon is converted into signal and idler photons. Energy conservation gives $\omega_p = \omega_s + \omega_i$, where ω_p is the pump frequency, ω_s is the signal frequency, and ω_i is the idler frequency. For flux-pump designs, the pump frequency is approximately twice the signal frequency, $\omega_p \approx 2\omega_s$; thus, $\omega_i \approx \omega_s \approx \frac{1}{2}\omega_p$. The main advantage of this design is that the pump tone is largely detuned from the signal tone, so it is easy to filter downstream in the readout line such that the readout is not contaminated by the strong pump tone. The flux-pump design is being investigated for future research and development in ADMX.

JPAs are characterized in reflection via a transmission line, which carries the signal tone, the amplified signal, and the pump tone if it is current-pumped. A circulator is needed to route the input signal into the JPA and the amplified signal down the output line and to isolate the pump from reflecting off the cavity and interfering (Fig. 9). The performance of a JPA is controlled by tuning three parameters: flux bias, pump power, and the detuning of the pump tone from the signal frequency. At optimal performance, JPAs typically provide at least 20 dB of gain over tens of MHz of bandwidth. This was found to be true of the ADMX JPA after installation during run 1B. If a JPA adds the minimum amount of noise possible, then the SNR improvement of the amplifier is slightly lower than its power gain. Figure 18 shows UCB fabricated JPA tuning for optimized gain, increase in noise floor when the JPA is on, and noise temperature optimization as a function of different relevant parameters used at the UW for run 1B. This JPA was operated in the frequency range of 680–790 MHz.

5. Josephson Parametric Amplifier (JPA): Fabrication

JPAs are typically fabricated using electron-beam lithography to expose resist spun on top of a substrate. First, large structures such as parallel plate capacitors, geometric inductors, and RF launches are defined, typically in a lift-off process. Then, Josephson junctions, most commonly of the superconductor–insulator–superconductor (S–I–S) variety, are added. The insulating barrier is typically made of a thermally grown oxide (e.g., Al–AlOx–Al, as is the case for the ADMX JPAs). After exposure and development, a double-angle evaporation was used to deposit a thin film of aluminum and the first layer is allowed to oxidize before depositing the second layer. This method is sometimes referred to as the Niemeyer–Dolan technique

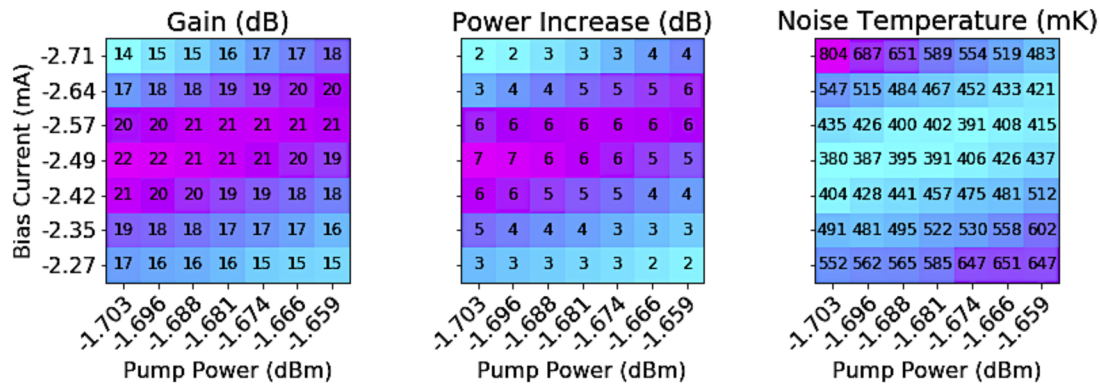


FIG. 18. A typical SNRI scan used during operations to select the optimal JPA parameters. Reprinted with permission from Bartram *et al.*, Phys. Rev. D **103**, 032002 (2021). Copyright 2021 American Physical Society. Left: Gain denoted by the difference in traces between JPA pump on and off states. Center: The increase in power between JPA pump on and off states. Right: The resultant noise temperature from the combination of the two measurements and the known noise temperature of the downstream electronics. In this case, a bias of -2.49 mA and a pump power of -1.703 dBm (< -100 dBm on chip) with a system noise temperature of 380 mK were selected as best for the data-taking cycles in that measurement bandwidth.

for fabricating very small overlapping structures. For a full explanation of this technique, the reader is referred to Ref. 55. For an image of a full JPA chip and enlarged images of the smaller structures, such as the SQUIDS and Josephson junctions, see Fig. 19.

E. Dilution refrigerator

ADMX uses a dilution refrigerator as the final cooling stage of the detector. Cooling is provided by the circulation of ^3He for the ^3He -rich phase to a dilute phase in the mixing chamber of the refrigerator. The rate is controlled by heater in the still chamber, which evaporates ^3He from the dilute phase to the gas phase, which is almost pure ^3He .

The dilution refrigerator (Model JDR-800) was custom built by Janis Research Company.⁵⁶ Based on the anticipated heat loads of operating the haloscope, it was designed to have $750 \mu\text{W}$ of cooling power at 100 mK. An actively driven still heater was used to control the ^3He flow rate. A pumped ^4He refrigerator pre-cools ^3He returned to the dilution refrigerator before it enters the still chamber, which is pumped by a Pfeiffer CombiLineTM, Model WS1250WA

(OKTA-2000/A100L) oil-free pumping station. Root pumps use Fomblin[®] oil to reduce hydrogen sources in the dilution refrigerator system. At room temperature, LN2 traps and a hydrogen getter (MC1500902F from saesgroup Pure Gas) were used to clean the mixture. A gold-plated intermediate plate was used to bolt the cavity and cryogenic electronics tower to the mixing chamber of the refrigerator to ensure good thermalization. The attachment of the cavity to the dilution refrigerator mixing chamber is shown in Fig. 20.

F. Sidecar: A high frequency prototype

Ultimately, we want to operate ADMX at higher frequencies of several GHz to probe higher mass axions. As a preliminary test, we allocated a small amount of space inside the insert to operate Sidecar (Fig. 21). Sidecar operated a 4–6 GHz cavity in the TM_{010} mode and has been used to demonstrate that data can be taken on the TM_{020} mode. Sidecar can take data all the way up to 7.2 GHz. One of the main differences between Sidecar and the ADMX main cavity is that Sidecar is tuned using attocube piezo-electric actuators.⁵⁷

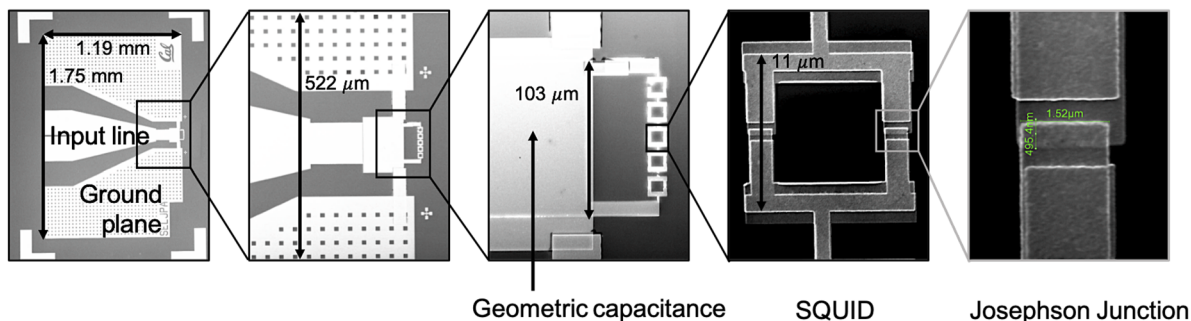


FIG. 19. JPA chip. The input line and ground plane form a coplanar waveguide leading to an array of five SQUIDS, which is shunted by a large parallel plate capacitor. The dimensions of a typical Josephson junction can be precisely fabricated on the order of tens to hundreds of nanometers. From left to right, the images are increasingly enlarged to show the array of SQUIDS and Josephson junction.

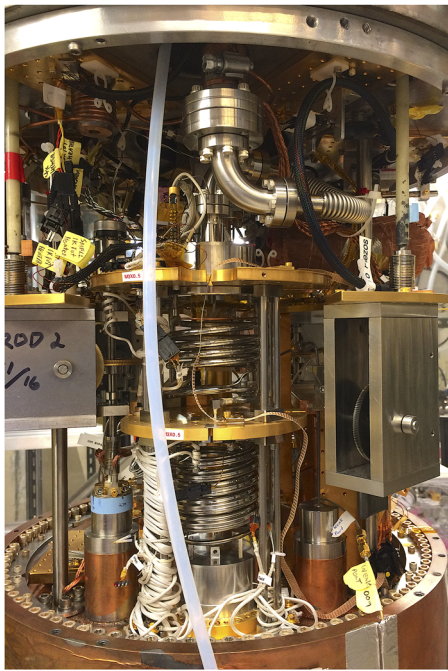


FIG. 20. Dilution refrigerator bolted to the microwave cavity (rim of the cavity top shown).

Consequently, it is a prototype test-bed for the future motion control system for the main cavity. The attocube actuators are less bulky and dissipate less heat than the currently used stepper motors and will be implemented in future ADMX runs. In its location on top of the ADMX cavity, Sidecar experiences a mean field that is one-half that of the main cavity. Thus, Sidecar also acts as a fully operational

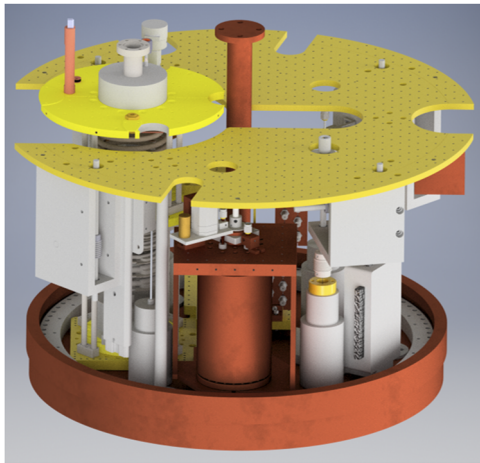


FIG. 21. CAD rendering of the Sidecar cavity *in situ* between the larger main cavity top plate (bottom) and the 1 K plate (top). The cavity and piezo-electric actuators are thermally sunk to the top of the Sidecar cavity, and the large copper support frame minimizes thermal spikes associated with actuators stepping.

haloscope operating at higher frequency. For further information on the Sidecar cavity, see Ref. 13.

IV. HELIUM LIQUEFACTION SYSTEM AND INFRASTRUCTURE

To meet the high liquid ^4He demands of the two solenoid magnet systems and the two 1 K pots for the dilution refrigerator mixture condensing line and cavity thermal shields, a Linde L1410 ^4He liquefaction system was installed at CENPA, which includes a closed loop system of the liquefier, rotary screw compressor, screw compressor, and two Bauer compressors. Any helium vapor produced by the system is collected into a gas bag with a volume sufficient to hold 19 000 l of ^4He gas at STP equivalent to 25 l of liquid. From the gas bag, a screw compressor was used to compress the gaseous ^4He into a medium pressure tank up to 10^6 N/m 2 . The medium pressure helium is then regulated into a pair of Bauers high pressure compressors to a system of 12, 1.4 m tall and standardized high pressure rated cylinders (T-bottles) up to 10^7 N/m 2 . These T-bottles supply the L1410 liquefier with the required high pressure helium via two T-bottles acting as a surge tank to quell any instabilities in the supply pressure.

The liquefier produces 15–45 l of ^4He per hour depending on whether liquid nitrogen pre-cooling is used and the purity of helium flowing into the purifier of the liquefier. From the liquefier, ^4He is routed via a remote delivery tube (RDT) to a Mother Dewar of 2500 l capacity. Stored ^4He is then transferred into either the main magnet or a reservoir. In addition, the University of Washington CENPA's cryogen infrastructure includes a large liquid nitrogen (LN2) tank that is used to provide LN2 for dilution refrigerator traps and to provide a 77 K thermal shield for the main ADMX magnet.

V. DAQ INFRASTRUCTURE AND WARM ELECTRONICS

The data acquired for ADMX can be divided into periodically sampled experimental state information and RF measurements taken during the axion search. The experimental state information consists of readings from temperature, pressure, magnetic field, and current sensors, which will be discussed in Sec. V A.

A. Sensors

For temperatures above 1 K, we used an assortment of platinum resistance (Lakeshore PT-102), Cernox (Lakeshore CX-1010 and CX-1050), and ruthenium oxide (Lakeshore RX-102 and RX202) sensors for readout. Sensor resistances were measured by performing four-wire resistance measurements with an Agilent multifunction measure unit. For temperatures below 1 K, resistance measurements were made with a Lakeshore 370 Alternating Current (AC) resistance bridge.⁵⁸ To ensure minimum heating of the sensors, the excitation voltage from the resistance bridge was reduced until it had no noticeable effect on the resulting temperature measurement (while still maintaining a high enough voltage to minimize noise). For temperature sensors at the 100 mK stage of the experiment, the excitation voltage that minimized heating was 20 μV . In run 1A, the temperatures of the cavity and quantum electronics package were measured using Cernox temperature sensors (Lakeshore CX-1010), while the temperature of the mixing chamber mounted to the cavity was measured using a ruthenium oxide temperature sensor

(Scientific Instruments RO600). During operations, we observed that the Cernox sensors had a large magneto-resistance at temperatures below 1 K. When the magnet was ramped to 6.8 T, it was observed that temperature readings on the Cernox temperature sensors on the cavity increased by 70% compared to the ruthenium oxide temperature sensor on the mixing chamber, which increased by 2%. Thus, in run 1A, the temperature of the cavity was determined by using the ruthenium oxide temperature sensor mounted to the mixing chamber. Because the quantum electronics package was kept in a field-free region, the Cernox temperature sensors located on the package did not suffer from magnetic field effects and were used to measure the physical temperature of the quantum amplifier.

In run 1B, the Cernox sensors on the cavity and quantum amplifier package were replaced with ruthenium oxide sensors (Scientific Instruments RO-600).

The vacuum insulation space between the insert and the magnet bore was monitored with an ionization gauge, which is kept below 10^{-7} Torr during operation. When the main magnetic field is changed, the magnetic field cancellation near the quantum electronics was monitored by Hall probe measurements, but these probes were not energized during data-taking due to the excess heat they generated.

B. RF chain and run cadence

Thermal power from the cold space was amplified by using a chain of amplifiers with the following approximate characteristic gains: quantum amplifiers (Fig. 8, MSA, and Fig. 9, JPA), 20–30 dB, HEMT amplifiers 30 dB, and a series of room temperature amplifiers (Minicircuit), 40 dB. This power was directed with a custom switch box (Fig. 22) to a variable-frequency superheterodyne receiver (Fig. 23).

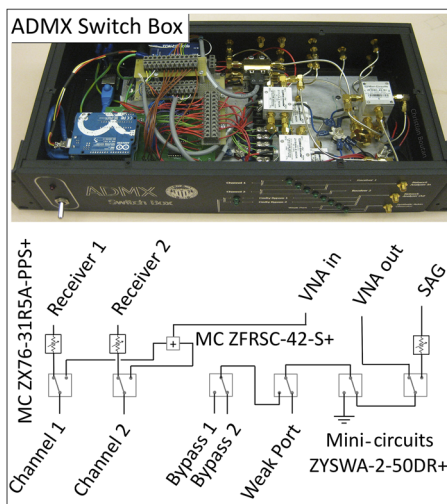


FIG. 22. Custom ADMX switch box that has been directing RF traffic since 2013. Signals from the vector network analyzer or synthetic axion generator are sent to either the weakly coupled antenna or bypass lines used for antenna coupling measurements. Signals from the cavity are directed to either the ambient temperature receiver or back to the network analyzer. Programmable attenuators allow the option to easily correct for receiver compression, digitizer clipping, or cavity input power.

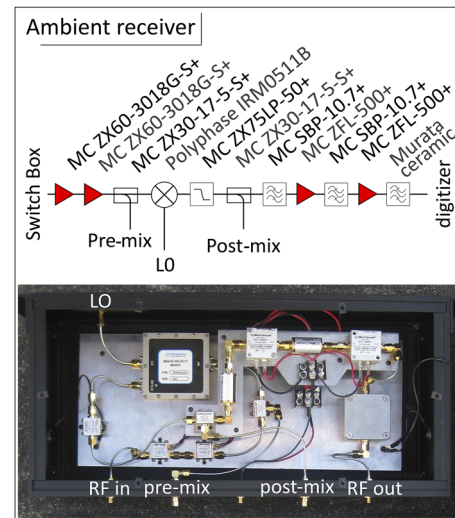


FIG. 23. Ambient receiver built for signal extraction using the TM_{010} mode. The signal is amplified, mixed to 10.7 MHz using an image reject mixer, and bandpass filtered.

This ambient receiver mixed the signal down to 10.7 MHz using a Polyphase image reject mixer to remove the higher frequency sideband. Additional amplification compensated for loss along the chain, and antialiasing, narrow bandpass filters centered on 10.7 MHz ensured the removal of harmonics. The signal was then time series digitized at 200 MegaSamples/s with an 8 bit digitizer (Signatech). In software, this signal was digitally mixed down again and filtered, retaining the power spectrum with a bandwidth of 25 and 50 kHz in runs 1A and 1B, respectively. If detected, an axion signal would appear as an excess in this power spectrum or as a nearly coherent oscillation in the time series.

A Keysight E5071C vector network analyzer (VNA) was used to make active measurements of the RF system. It sent frequency-swept signals through the switch box (Fig. 22) to the weakly coupled cavity port and measured the complex response of signals transmitted through the cavity (S_{21}) and off the antenna (S_{11}). Transmission measurements (Figs. 8 and 9) provided information about the cavity mode structure and the frequency and Q of the TM_{010} mode. Knowledge about the antenna coupling was obtained with reflection measurements and performed by directing swept power through a bypass line and circulator to the antenna. When critically coupled, on resonance power was absorbed by the cavity. Off-resonance, the signal was reflected off the antenna and up through the receiver chain (see Figs. 6, 8, and 9). This off-resonance baseline was also used for wide-band measurements of the system gain for noise calibrations.

The data-taking process is fully automated via custom DAQ software tools that provide a number of useful features, such as remote monitoring of state information. The lowest layer of the DAQ software is based on Experimental Physics and Industrial Control System (EPICS),⁵⁹ which provides a uniform software interface for interaction with the instruments. As data are acquired through EPICS, they are periodically logged in a SQL database. The on-site

database is synchronized with an off-site database mirror that allows for backup and analysis access.

The experiment was automated through a series of scripts written in Lua.⁶⁰ These scripts controlled the serial measurements made during the course of normal operations. Individual scripts customized for a specific task could also be developed for the purpose of engineering studies throughout the run. During the course of a run, experiment operators interacted with the DAQ software through a web interface that enabled remote monitoring and plotting of experimental state information.

C. Synthetic axion generator

RF signals that were indistinguishable from an isothermally modeled axion signal were injected into the experiment through the weakly coupled port in the cavity to ensure the robustness of the experiment in detecting axions. Known as synthetic axions, these signals were generated using an arbitrary waveform generator (Keysight AG33220A), which produced a Maxwell–Boltzmann (MB)-like line shape ~ 500 Hz in width. This signal was then mixed up to hundreds of MHz frequencies corresponding to the search range of ADMX. The injected power was varied by changing the output power of the arbitrary function generator and calibrated to the range of power predicted for QCD axions within the experiment. The synthetic axion injection system was implemented in runs 1A and 1B with a blind injection scheme in run 1B to introduce artificial axion candidates into the data.

D. System noise temperature

The detectability of an axion signal depends on the magnitude of the noise background. Because the background is almost entirely thermal noise, it is of paramount importance to understand the system noise temperature, which includes thermal fluctuations from the photon occupation of the cavity, power fluctuations due to amplification electronics, and attenuation that decreases the SNR. It should be noted that the contribution to the system noise from the fluctuation of photon occupation of the cavity is given by the fluctuation–dissipation theorem or generalized Nyquist theorem⁶¹ as

$$P_n = k_B T b \left(\frac{hf/k_B T}{\exp(hf/k_B T) - 1} \right) + \frac{hf b}{2}. \quad (9)$$

Here, k_B is the Boltzmann constant, T is the physical temperature of the thermal source, b is the bandwidth over which the noise is measured, h is Planck's constant, and f is the frequency. The first term in the equation corresponds to the thermal noise power radiated into a single waveguide mode by a blackbody. The second term denotes the zero point fluctuation noise.⁶² In the thermal limit $hf \ll k_B T$, P_n converges to $k_B T b$ and the background noise contribution arises solely from the physical temperature of the cavity. From Eq. (5), the system noise temperature T_{sys} can be defined such that the ratio of the signal power of an axion signal coming from the cavity with a bandwidth b to nearby background noise Gaussian power is

$$SNR = \frac{P_{a \rightarrow \gamma\gamma}}{k_B T_{sys} b}. \quad (10)$$

It is important to recall the following two equations: The noise from a thermal source of temperature T followed by an amplifier with gain G and noise T_a is equivalent to a thermal source with equivalent noise temperature⁶³

$$GT_{equiv} = G(T + T_a), \quad (11)$$

while a thermal source of temperature T followed by an attenuation α held at temperature T_a is equivalent to a thermal source with equivalent noise temperature

$$T_{equiv} = \alpha T + T_a(1 - \alpha). \quad (12)$$

These two equations can be combined for an arbitrary cascade of components; in general, the earlier stage components such as the first-stage amplifiers have a more significant effect on the equivalent noise than that of later stage components.

In the ADMX setup described in Figs. 8 and 9 far from resonance, where the cavity is reflective, the primary source of thermal noise is attenuator A. Near resonance, the thermal noise power is a combination of the power radiated at A and the power radiated from the cavity. In the case of critical coupling, the entire initial thermal noise comes from the cavity. Beyond the cavity, there are contributions from the attenuation between the cavity and the first-stage amplifier, the first-stage amplifier (MSA or JPA), the attenuation between the first- and second-stage amplifiers, and finally the second-stage amplifier (HEMT). Beyond the second-stage amplifier, the noise contributions of the receiver components are minor.

Now, we will discuss several *in situ* noise measurements from these various components in the RF chain.

1. Heated load measurements

A heated load measurement refers to physically changing the temperature of one part of the system while monitoring the power over a certain bandwidth. The system noise can be divided into two components: the part that varies with the physical temperature and the part that does not. In ADMX, the performance of the JPA and MSA was extremely sensitive to the physical temperature so that a heated load measurement including the first-stage amplifier proved unreliable. Two alternative configurations were found, however, both reliable and useful to measuring the system noise temperature. In the first configuration, the first-stage amplifier was disabled or bypassed and the temperature of the mK electronics (switch and circulators) was varied, while the power far from resonance was measured. In this case, the measured power is

$$P \propto T_m + T_h, \quad (13)$$

where T_m is the temperature of the mK electronics and T_h is the noise contribution of the HEMT and downstream electronics. An example of this measurement is shown in Fig. 24.

In the second configuration, the RF system switch, shown in Figs. 8 and 9, was switched to the hot load. The temperature of the load could be varied independently from the temperature T_m of the mK electronics stage. In this case, the output power can be expressed as

$$P \propto \alpha T_L + (1 - \alpha) T_m + T_h, \quad (14)$$

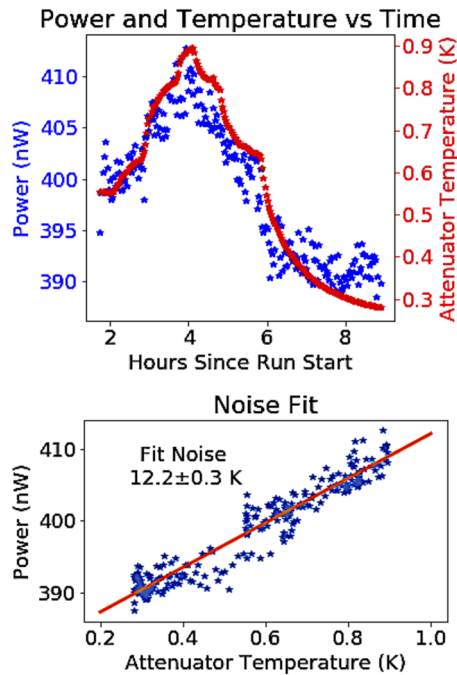


FIG. 24. An example of the noise measurement of the HEMT at 705 MHz performed by heating the mK (switch and circulators) space. The top panel shows the heating and cooling of the mK space, whereas the bottom panel shows the noise fit to the heating and cooling process. These measurements were performed four times during data-taking, every 5 MHz throughout the frequency band covered. They were consistent with uniform noise performance across the band.

where T_L is the temperature of the load, α is the attenuation of all of the components in the mK electronics stage, and T_h is the noise contribution of the HEMT and downstream electronics. Both of these configurations were used in runs 1A and 1B for noise temperature studies of the HEMTs.

2. Signal-to-noise improvement measurements

The Signal-to-Noise Ratio Improvement (SNRI) measurement is commonly used in characterizing the performance of ultra-low noise amplifiers. To perform a SNRI measurement, one measures the total system gain and power output in the desired frequency band with the amplifier included and excluded from the RF chain (Figs. 8 and 9). The ratio of the system noise of the RF system with the amplifier included (T_{included}) to the system noise with the amplifier excluded (T_{excluded}) is

$$\frac{T_{\text{included}}}{T_{\text{excluded}}} = \frac{G_{\text{excluded}} P_{\text{included}}}{G_{\text{included}} P_{\text{excluded}}}. \quad (15)$$

Here, G_{excluded} (G_{included}) is the gain when the amplifier is excluded (included); similarly, P_{included} (P_{excluded}) is the measured power when the amplifier is included (excluded).

An SNRI measurement of the first-stage amplifier combined with the heated load measurement of the HEMT and downstream noise yields the total system noise. The values of variables involved in obtaining the SNRI-like gain and power increase are shown in Fig. 18 as a function of various amplifier bias parameters, such as

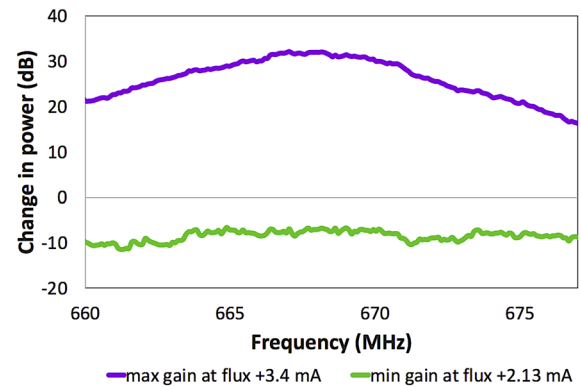


FIG. 25. Change in power as seen with a network analyzer when the MSA flux was optimized to yield the maximum gain (violet) and minimum gain (green) for the constant bias values of current and varactor voltage. This difference between the violet and green curve was subtracted from the gain of the MSA to obtain the SNR increase used in the noise temperature analysis.

current and pump power for the JPA. In addition, the system noise temperature is also shown as a function of pump power bias values.

In the case of the MSA in run 1A, switching it out of the signal path required actuating two switches shown in Fig. 8, which changed the MSA temperature significantly and impeded proper performance. Therefore, the power and gain with the MSA switched out were measured infrequently, introducing uncertainty into the measurement of the overall system gain or output power varied over time. However, SNRI measurements could also be made by comparing minimum and maximum power transmitted through the MSA by changing the flux bias while keeping the current and varactor biases constant. An example of this is shown in Fig. 25.

In the case of the JPA in run 1B, since the JPA acts as a perfect reflector when the pump tone is disabled, the total SNRI could be measured very quickly with the pump on and off (Fig. 26). Combined with a heated load HEMT measurement, this procedure provided a reliable and immediate measurement of the system noise temperature.

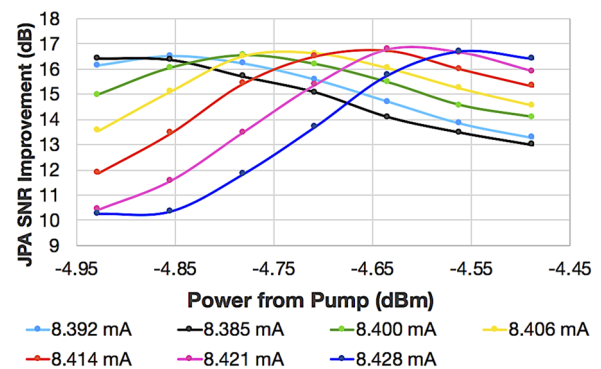


FIG. 26. JPA SNR improvement as a function of the absolute JPA pump tone at different flux bias values denoted in mA corresponding to different colors. The lines connect the individual points. After the JPA was biased for optimal gain through small steps of flux values, the SNR increase was optimized by scanning through various pump tones.

3. On-off-resonance measurements

In runs 1A and 1B, the physical temperature of the cavity was significantly different from the physical temperature of the mK electronics. The former was close to 150 (130 mK) for run 1A (1B), and the latter was close to 300 (250 mK) for run 1A (1B). The relative thermal power on- and off-resonance encoded sufficient information to determine the system noise in the same way as a heated load measurement. Provided that the attenuation in the mK electronics space, α , could be determined and there were no reflections in the system, the expected noise power entering the first-stage amplifier was

$$P \propto (1 - \alpha)T_m + \alpha[(1 - \Gamma)T_c + \Gamma((1 - \alpha)T_m + \alpha T_a)], \quad (16)$$

where T_a is the physical temperature of attenuator A in Fig. 8, T_c is the physical temperature of the cavity, and $\Gamma(f)$ is the reflection coefficient of the cavity near resonance. If the antenna is critically coupled, $\Gamma(f)$ is zero on resonance and unity far from resonance. Small reflections within the passive components in the mK space could distort this shape, but an overall fit of a more sophisticated model to the power as a function of frequency enabled us to extract T_{sys} using temperature sensor measurements of T_m , T_a , and T_c .

4. Run 1A noise temperature

In practice, a combination of the above measurements yields a reliable system noise temperature. In run 1A, the switch for the heated load malfunctioned, so all noise calibration measurements came from the “on-off-resonance” method. Typical parameters for this measurement were as follows: the noise contribution off-resonance of 300 mK, the noise contribution coming from the cavity and accounting attenuators of 100 mK, and a dip of order 20% in power seen at the cavity resonance in Fig. 27. This measurement yielded a system noise temperature of order 500 mK for the run and was measured at several frequencies. There was significant variation in the system noise over frequency due to different gains of

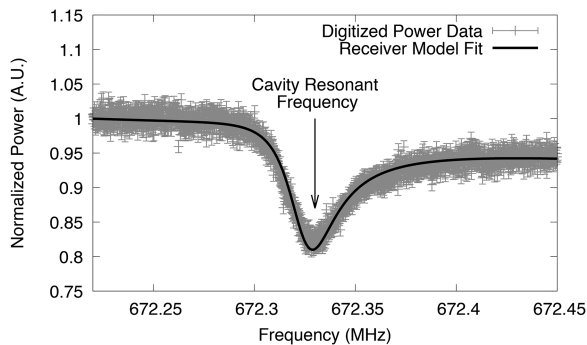


FIG. 27. On-off-resonance measurement for run 1A.²⁶ Reproduced with permission from Du *et al.*, Phys. Rev. Lett. **120**, 151301 (2018). Copyright 2018 Author(s), licensed under a Creative Commons Attribution 4.0 license. The power is the sum of the 300 mK physical temperature of an attenuator and the receiver noise temperature. On resonance, the power is the sum of the 150 mK physical temperature of the cavity and the receiver noise temperature. The noise power on- vs off-resonance acts as an effective hot-cold load, with the physical temperatures measured with sensitive thermometers. The asymmetry of the shape is a result of interactions between components, as described in Ref. 26.

the MSA. This variation was tracked by a SNRI measurement before each 100 s digitization using a network analyzer transmission measurement to track the gain and the average power in the digitization itself to track the noise power. More information on this is available in Ref. 26.

5. Run 1B noise temperature

In ADMX run 1B, the hot load had an unintentional touch to the same temperature stage as the cavity and the mK temperature compared to run 1A so that the on-off-resonance method could not be used effectively. We constructed a model with attenuation through mK electronics α (which included circulators C_1 , C_2 , and C_3 , along with any line losses between components) and noise temperature of the HEMT amplifier as free parameters. In addition, we used the hot load temperature T_L and the mK electronics temperature T_m , which we could measure and change independently. This model was simultaneously fit to measurements where the hot load was heated and where the cryogenic electronics package's temperature was changed. The hot load and heated cryogenic electronics package's measurements were fit to Eq. (14). This yielded the system noise temperature with the JPA without the pump power. It is helpful to recognize that the total loss α can be decomposed into the loss between the cavity and JPA, α_{C-J} , and the loss between the JPA and the HEMT, α_{J-H} , such that $\alpha = \alpha_{J-H}\alpha_{C-J}$. Because the components and line lengths are similar, $\alpha_{J-H} \approx \alpha_{C-J}$.

We made an SNRI measurement frequently throughout the data run. The system noise with the JPA energized was

$$T_{sys,JPA} = T_{sys,HEMT} \frac{P_{JPA}}{P_{HEMT}} \frac{1}{\alpha_{J-H} G_{JPA}}. \quad (17)$$

We derived this from Eq. (15), noting that the JPA gain must be weighted by the attenuation between the JPA and the HEMT. The power and gain of JPA (P_{JPA} , G_{JPA}) and HEMT (P_{HEMT} , G_{HEMT}) can be measured directly, but the uncertainty in how much of the loss is distributed upstream and downstream of the JPA leads to some uncertainty on this system noise as considered at the JPA input. However, to calculate the equivalent system noise from a signal generated in the cavity (such as an axion), the system noise as measured at the JPA input must take into account the attenuation between the cavity and the JPA, which reduces the signal and replaces it with thermal noise from the attenuator, yielding

$$\begin{aligned} T_{sys,Cavity} &= T_{sys,HEMT} \frac{P_{JPA}}{P_{HEMT}} \frac{1}{(\alpha_{J-H}\alpha_{C-J})G_{JPA}} \\ &= T_{sys,HEMT} \frac{P_{JPA}}{P_{HEMT}} \frac{1}{\alpha G_{JPA}}. \end{aligned} \quad (18)$$

Thus, the uncertainty in distribution of loss/attenuation does not significantly affect uncertainty in the system noise as compared to the signal in the cavity.

Typical measurements for run 1B were $\alpha = 3.27 \pm 0.08$ dB and a noise temperature at the HEMT input of 8.16 ± 0.11 K. These were independent of frequency below 770 MHz. The ideal noise temperature of HEMT is notably lower (2 K) in the component datasheet, indicating the possibility that the HEMT noise was adversely affected by the magnetic field, an effect studied in Ref. 64. SNRI measurements varied between 13 and 16 dB during the data run (Fig. 26)

depending on frequency, amplifier bias conditions, and the physical temperature of the amplifier and the cavity. This yielded noise temperatures of 350–500 mK.

Above 770 MHz, the transmission coefficient of the circulators decreased, increasing α and thus yielding slightly higher system noise temperature. The increase in α was 3 dB at 800 MHz, consistent with both the component datasheet and separate cold measurements of the circulators. This additional attenuation caused a proportional increase in system noise temperature.

VI. DATA ANALYSIS

After acquiring the information regarding the experimental state through sensors and determining the system noise temperature, we analyzed the data by combining the individual 100 second power spectra collected into a cumulative “grand spectrum,” which we used to search for axion-like signals. The details of the analysis procedure vary between runs, but the general steps follow those outlined in Ref. 65. First, the background receiver shape in the individual scans is filtered out. In run 1A, the background receiver shape was removed by applying a Savitsky–Golay filter (length 121 and polynomial order 4) to 95% of the least-deviant power bins.²⁶ In run 1B, a six-order Padé filter was used to remove the background.²⁸ The filtered power spectra were then scaled to the system noise temperature, and individual bins of the spectra were weighted by their difference from the cavity’s resonant frequency via the Lorentzian line shape. This produced a spectrum of the excess power due to a potential axion signal. Each of these filtered and weighted scans were then combined into a single grand spectrum representing the excess power from the cavity across the entire frequency range covered in each run. The grand spectrum was then used to search for axion-like signals by a convolution with two different axion signal shapes: a boosted Maxwell–Boltzmann shape predicted from the standard halo model for axion dark matter, as described in Ref. 66, and a signal shape predicted from N-body simulations described in Ref. 67. Data were taken usually in the order of 10 MHz wide “nibbles.” After an initial sweep in frequency, any axion-like signals were flagged as possible axion candidates and were re-scanned (usually within a week of the original scan). Re-scanning of candidates consisted of tuning the cavity to the frequency of the candidate and integrating for a significantly longer time to improve the expected signal-to-noise for a possible axion signal. Any signals that persisted following the re-scan were subjected to individual analysis, as detailed in Refs. 26, 27, and 68 before moving to the next “nibble.”

A medium-resolution and high-resolution channel enabled the search of virialized and non-virialized axions, respectively. Virialized axions are defined as having been gravitationally thermalized and are expected to follow a Maxwell–Boltzmann line shape (though other lineshapes are studied as well⁶⁷) with a spectral width on the order of 1 kHz.⁶⁹ Analyses of the medium-resolution channel were undertaken in Refs. 26 and 28. A more detailed outline of the analysis procedure that uses the medium-resolution channel and a second line shape derived from the N-body simulations described is found in Ref. 68. Non-virialized axions, on the other hand, have not reached a steady state of motion. Axions would be non-virialized if they have only recently entered the galactic halo or have been pulled out of tidally disrupted subhalos.⁶⁹

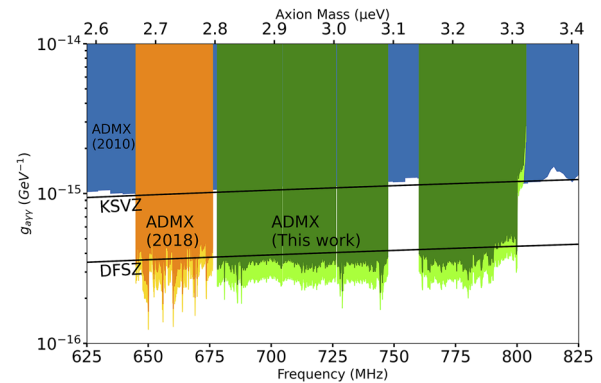


FIG. 28. Recent limits set by runs 1A and 1B.²⁷ Reproduced with permission from Du *et al.*, Phys. Rev. Lett. **124**, 101303 (2020). Copyright 2020 Author(s), licensed under a Creative Commons Attribution 4.0 license. 90% confidence exclusion on the axion–photon coupling as a function of axion mass for the Maxwell–Boltzmann (MB) dark matter model (dark green) and N-body model (light green) from Ref. 27. Blue and orange denote limits reported in Refs. 70 and 26, respectively.

VII. EXPERIMENTAL SENSITIVITY

With the above discussed hardware upgrades and analysis techniques, including the system noise temperature determination, ADMX was able to achieve DFSZ sensitivity in run 1A in 2017. In this run, axion masses covering 2.66–2.81 μeV corresponding to the frequency range of 645–680 MHz were probed using the MSA technology. The results are highlighted in Ref. 26. Similarly, in run 1B in 2018, we were able to maintain the DFSZ sensitivity while probing axion masses from 2.81 to 3.31 μeV corresponding to 680–790 MHz using the JPA technology. This was an improvement of about a factor of three in the frequency coverage from run 1A in 2017. A detailed summary of these results is plotted in Fig. 28.²⁷ These results were a factor of 7 improvement in the sensitivity compared to results from 2010.⁷¹ To date, ADMX is the only axion dark matter experiment that has achieved this sensitivity.

VIII. FUTURE AND CONCLUSION

While ADMX has made progress in ultra-low noise detector development technology for axion dark matter searches, much of the QCD axion parameter space still remains unexplored.

As it stands, ADMX uses a single cavity to probe for axions in the 2.4–6.2 μeV (580–1.5 GHz) range. Subsequent phases will search for 6.2–40 μeV (1.5–10 GHz) axions, requiring microwave cavities of smaller volume. To compensate for the reduced signal power deposited in a smaller cavity from axions, multiple cavities will be used that tune together in frequency. This strategy trades a small volume, yielding reduced sensitivity to axions for the added complexity of frequency-locking multiple cavities at each axion detection frequency step.

The first ever four-cavity array proof of concept for ADMX was tested in the work of Ref. 72. A four-cavity array prototype was implemented at UF to provide a testbed for a multi-cavity array for the ADMX. Designed for a frequency range of 4.4–6.3 GHz, the prototype array uses a cavity cross section that is roughly 1:3 scale to that of the planned full size experiment, which will achieve resonances in the range of 1–2 GHz. The principal design challenge of a

multi-cavity system is to maintain a frequency lock between the cavities in order to use the array as a single higher frequency cavity that exploits the maximum volume possible within the ADMX magnet bore. A preprint discussing the details of this design and challenges is in progress.

In the near future, there are two potential enhancements being developed in parallel to increasing the scan rate: the first is exploring the increasing cavity quality factor by employing superconducting cavities⁷³ that can maintain their low RF-losses in a high magnetic field and the second is to explore squeezing technique⁷⁴ to lower noise beyond the quantum limit, which from 2 to 4 GHz rises from 100 to 200 mK and begins to dominate the thermal noise of the ADMX system. With these enhancements, ADMX hopes to cover several GHz in frequency over the next few years. Needless to say, systems operating in lower than the quantum-noise-limit is a must before the search can be extended to higher axion mass in a reasonable amount of time. Therefore, superconducting Josephson junction based single photon sensors that count photons thereby eliminating the quantum-noise-limit seem to be a promising avenue to pursue. Furthermore, significant strides in technological advancement are necessary before the complete QCD axion parameter space can be examined.

ACKNOWLEDGMENTS

The authors are part of the ADMX collaboration. This research was supported by the U.S. Department of Energy through Grant Nos. DE-SC0009723, DE-SC0010296, DE-SC0010280, DE-SC0010280, DE-FG02-97ER41029, DE-FG02-96ER40956, DE-AC52-07NA27344, DE-C03-76SF00098, DE-SC0009800, and DE-SC00116655. This paper was written by Fermi Research Alliance, LLC, under Contract No. DE-AC02-07CH11359 with the U.S. Department of Energy, Office of Science, Office of High Energy Physics. Support from the Heising-Simons Foundation along with Lawrence Livermore and Pacific Northwest National Laboratories LDRD is also acknowledged (Report Nos. FERMILAB-PUB-20-331-AD-E-QIS, LLNL-JRNL-814312, and PNNL-SA-154970).

AUTHOR DECLARATIONS

Conflict of Interest

The authors have no conflict of interest to disclose.

DATA AVAILABILITY

The data that support the findings of this study are available from the corresponding author upon reasonable request.

REFERENCES

- J. Preskill, M. B. Wise, and F. Wilczek, *Phys. Lett. B* **120**, 127 (1983).
- L. F. Abbott and P. Sikivie, *Phys. Lett. B* **120**, 133 (1983).
- M. Dine and W. Fischler, *Phys. Lett. B* **120**, 137 (1983).
- J. Ipser and P. Sikivie, *Phys. Rev. Lett.* **50**, 925 (1983).
- R. D. Peccei and H. R. Quinn, *Phys. Rev. Lett.* **38**, 1440 (1977).
- R. D. Peccei and H. R. Quinn, *Phys. Rev. D* **16**, 1791 (1977).
- P. Sikivie, *Lect. Notes Phys.* **741**, 19 (2008); [arXiv:astro-ph/0610440](#) [astro-ph].
- M. P. Hertzberg, M. Tegmark, and F. Wilczek, *Phys. Rev. D* **78**, 083507 (2008).
- C. Bonati, M. D'Elia, M. Mariti, G. Martinelli, M. Mesiti, F. Negro, F. Sanfilippo, and G. Villadoro, *J. High Energy Phys.* **2016**, 155.
- E. Berkowitz, M. I. Buchoff, and E. Rinaldi, *Phys. Rev. D* **92**, 034507 (2015).
- G. Ballesteros, J. Redondo, A. Ringwald, and C. Tamarit, *Phys. Rev. Lett.* **118**, 071802 (2017).
- S. J. Asztalos, G. Carosi, C. Hagmann, D. Kinion, K. van Bibber, M. Hotz, L. J. Rosenberg, G. Rybka, A. Wagner, J. Hoskins, C. Martin, N. S. Sullivan, D. B. Tanner, R. Bradley, and J. Clarke, *Nucl. Instrum. Methods Phys. Res., Sect. A* **656**, 39 (2011).
- C. Boutan, M. Jones, B. H. LaRoque, N. S. Oblath, R. Cervantes, N. Du, N. Force, S. Kimes, R. Ottens, L. J. Rosenberg, G. Rybka, J. Yang, G. Carosi, N. Woollett, D. Bowring, A. S. Chou, R. Khatriwada, A. Sonnenschein, W. Wester, R. Bradley, E. J. Daw, A. Agrawal, A. V. Dixit, J. Clarke, S. R. O'Kelley, N. Crisosto, J. R. Gleason, S. Jois, P. Sikivie, I. Stern, N. S. Sullivan, D. B. Tanner, P. M. Harrington, and E. Lentz (ADMX Collaboration), *Phys. Rev. Lett.* **121**, 261302 (2018).
- S. Weinberg, *Phys. Rev. Lett.* **40**, 223 (1978).
- F. Wilczek, *Phys. Rev. Lett.* **40**, 279 (1978).
- A. Vainshtein, M. A. Shifman, and V. I. Zakharov, *Nucl. Phys. B* **166**, 493 (1980).
- J. E. Kim, *Phys. Rev. Lett.* **43**, 103 (1979).
- M. Dine, W. Fischler, and M. Srednicki, *Phys. Lett. B* **104**, 199 (1981).
- A. Zhitnitsky, *Sov. J. Nucl. Phys.* **31**, 260 (1980), see <https://www.osti.gov/biblio/7063072>.
- P. Sikivie, *Phys. Rev. D* **32**, 2988 (1985).
- R. H. Dicke, *Rev. Sci. Instrum.* **17**, 268 (1946).
- H. Peng, S. Asztalos, E. Daw, N. A. Golubev, C. Hagmann, D. Kinion, J. LaVeigne, D. M. Moltz, F. Nezrick, J. Powell *et al.*, *Nucl. Instrum. Methods Phys. Res., Sect. A* **444**, 569 (2000).
- R. G. Chambers, *Nature* **165**, 239 (1950).
- See <https://www.3ds.com/products-services/simulia/products/cst-studio-suite/> for CST studio suite; accessed 06 December 2019.
- C. Boutan, "A piezoelectrically tuned RF-cavity search for dark matter axions," Ph.D. thesis, University of Washington, 2017.
- N. Du, N. Force, R. Khatriwada, E. Lentz, R. Ottens, L. J. Rosenberg, G. Rybka, G. Carosi, N. Woollett, D. Bowring, A. S. Chou, A. Sonnenschein, W. Wester, C. Boutan, N. S. Oblath, R. Bradley, E. J. Daw, A. V. Dixit, J. Clarke, S. R. O'Kelley, N. Crisosto, J. R. Gleason, S. Jois, P. Sikivie, I. Stern, N. S. Sullivan, D. B. Tanner, and G. C. Hilton (ADMX Collaboration), *Phys. Rev. Lett.* **120**, 151301 (2018).
- T. Braine, R. Cervantes, N. Crisosto, N. Du, S. Kimes, L. J. Rosenberg, G. Rybka, J. Yang, D. Bowring, A. S. Chou, R. Khatriwada, A. Sonnenschein, W. Wester, G. Carosi, N. Woollett, L. D. Duffy, R. Bradley, C. Boutan, M. Jones, B. H. LaRoque, N. S. Oblath, M. S. Taubman, J. Clarke, A. Dove, A. Eddins, S. R. O'Kelley, S. Nawaz, I. Siddiqi, N. Stevenson, A. Agrawal, A. V. Dixit, J. R. Gleason, S. Jois, P. Sikivie, J. A. Solomon, N. S. Sullivan, D. B. Tanner, E. Lentz, E. J. Daw, J. H. Buckley, P. M. Harrington, E. A. Henriksen, and K. W. Murch (ADMX Collaboration), "Extended search for the invisible axion with the axion dark matter experiment," *Phys. Rev. Lett.* **124**, 101303 (2020); [arXiv:1910.08638](#) [hep-ex].
- R. C. Jaklevic, J. Lambe, A. H. Silver, and J. E. Mercereau, *Phys. Rev. Lett.* **12**, 159 (1964).
- J. Clarke and A. I. Braginski, *The SQUID Handbook: Fundamentals and Technology of SQUIDS and SQUID Systems* (Wiley VCH, Germany, 2004), Vol. 1.
- C. D. Tesche and J. Clarke, *J. Low Temp. Phys.* **29**, 301 (1977).
- W. C. Stewart, *Appl. Phys. Lett.* **12**, 277 (1968).
- D. E. McCumber, *J. Appl. Phys.* **39**, 3113 (1968).
- B. D. Josephson, *Phys. Lett.* **1**, 251 (1962).
- M. B. Ketchen and J. M. Jaycox, *Appl. Phys. Lett.* **40**, 736 (1982).
- M. Mück, M.-O. André, J. Clarke, J. Gail, and C. Heiden, *Appl. Phys. Lett.* **72**, 2885 (1998).
- M. Mück and J. Clarke, *J. Appl. Phys.* **88**, 6910 (2000).
- J. Clarke and A. I. Braginski, *The SQUID Handbook: Applications of SQUIDS and SQUID Systems* (Wiley VCH, Germany, 2006), Vol. 2.
- D. Kinion and J. Clarke, *Appl. Phys. Lett.* **98**, 202503 (2011).
- J. E. Sauvageau, C. J. Burroughs, P. A. A. Booii, M. W. Cromar, R. P. Benz, and J. A. Koch, *IEEE Trans. Appl. Supercond.* **5**, 2303 (1995).

- ⁴⁰S. R. O'Kelley, "The microstrip SQUID amplifier in the axion dark matter eXperiment (ADMX)," Ph.D. thesis, UC Berkeley, 2019.
- ⁴¹MA-COM, MA46H120 GaAs varactor (100 Chelmsford St., Lowell, MA 01851, USA).
- ⁴²M. Mück, B. Schmidt, and J. Clarke, *Appl. Phys. Lett.* **111**, 042604 (2017).
- ⁴³A. Roy and M. Devoret, *Phys. Rev. B* **98**, 045405 (2018).
- ⁴⁴A. A. Clerk, M. H. Devoret, S. M. Girvin, F. Marquardt, and R. J. Schoelkopf, *Rev. Mod. Phys.* **82**, 1155 (2010); [arXiv:0810.4729](https://arxiv.org/abs/0810.4729).
- ⁴⁵C. M. Caves, *Phys. Rev. D* **26**, 1817 (1982).
- ⁴⁶S. Wahlsten, S. Rudner, and T. Claeson, *J. Appl. Phys.* **49**, 4248 (1978).
- ⁴⁷B. Yurke, L. R. Corruccini, P. G. Kaminsky, L. W. Rupp, A. D. Smith, A. H. Silver, R. W. Simon, and E. A. Whittaker, *Phys. Rev. A* **39**, 2519 (1989).
- ⁴⁸N. A. Olsson, M. G. Oberg, L. D. Tzeng, and T. Cella, *Electron. Lett.* **24**, 569 (1988).
- ⁴⁹I. Siddiqi, R. Vijay, F. Pierre, C. M. Wilson, M. Metcalfe, C. Rigetti, L. Frunzio, and M. H. Devoret, *Phys. Rev. Lett.* **93**, 207002 (2004).
- ⁵⁰M. Hatridge, R. Vijay, D. H. Slichter, J. Clarke, and I. Siddiqi, *Phys. Rev. B* **83**, 134501 (2011).
- ⁵¹M. A. Castellanos-Beltran and K. W. Lehnert, *Appl. Phys. Lett.* **91**, 083509 (2007).
- ⁵²M. Sandberg, C. M. Wilson, F. Persson, T. Bauch, G. Johansson, V. Shumeiko, T. Duty, and P. Delsing, *Appl. Phys. Lett.* **92**, 203501 (2008).
- ⁵³T. Yamamoto, K. Inomata, M. Watanabe, K. Matsuba, T. Miyazaki, W. D. Oliver, Y. Nakamura, and J. S. Tsai, *Appl. Phys. Lett.* **93**, 042510 (2008).
- ⁵⁴M. A. Castellanos-Beltran, K. D. Irwin, G. C. Hilton, L. R. Vale, and K. W. Lehnert, *Nat. Phys.* **4**, 929 (2008).
- ⁵⁵D. H. Slichter, "Quantum jumps and measurement backaction in a superconducting qubit," Ph.D. thesis, University of California, Berkeley, 2011.
- ⁵⁶See <https://www.janis.com/Products/productsoverview/DilutionRefrigerators/StandardDilutionRefrigeratorSystems.aspx> for Janis standard dilution refrigerator systems; accessed 07 October 2019.
- ⁵⁷See <http://www.attocube.com/attomotion/> for Attocube, "Premium Line Introduction," 2018.
- ⁵⁸Lakeshore, User's Manual Model 370 AC Resistance Bridge, Lake Shore Cryotronics, Inc.
- ⁵⁹See <https://epics.anl.gov/base/index.php> for Experimental Physics and Industrial Control System; accessed 06 December 2010.
- ⁶⁰See <https://www.lua.org/manual/> for Lua Reference Manual; accessed 06 December 2010.
- ⁶¹H. B. Callen and T. A. Welton, *Phys. Rev. Lett.* **83**, 34 (1951).
- ⁶²I. A. Devyatov, L. S. Kuzmin, K. K. Likharev, V. V. Migulin, and A. B. Zorin, *J. Appl. Phys.* **60**, 1808 (1986).
- ⁶³H. T. Friis, *Proc. IRE* **32**, 419 (1944).
- ⁶⁴E. Daw and R. F. Bradley, *J. Appl. Phys.* **82**, 1925 (1997).
- ⁶⁵B. M. Brubaker, L. Zhong, S. K. Lamoreaux, K. W. Lehnert, and K. A. van Bibber, *Phys. Rev. D* **96**, 123008 (2017).
- ⁶⁶M. S. Turner, *Phys. Rev. D* **42**, 3572 (1990).
- ⁶⁷E. W. Lentz, T. R. Quinn, L. J. Rosenberg, and M. J. Tremmel, *Astrophys. J.* **845**, 121 (2017).
- ⁶⁸C. Bartram *et al.*, *Phys. Rev. D* **103**, 032002 (2021); [arXiv:2010.06183](https://arxiv.org/abs/2010.06183) [astro-ph.CO].
- ⁶⁹J. Hoskins, N. Crisosto, J. Gleason, P. Sikivie, I. Stern, N. S. Sullivan, D. B. Tanner, C. Boutan, M. Hotz, R. Khatriwada, D. Lyapustin, A. Malagon, R. Ottens, L. J. Rosenberg, G. Rybka, J. Sloan, A. Wagner, D. Will, G. Carosi, D. Carter, L. D. Duffy, R. Bradley, J. Clarke, S. O'Kelley, K. van Bibber, and E. J. Daw, *Phys. Rev. D* **94**, 082001 (2016).
- ⁷⁰S. Asztalos, E. Daw, H. Peng, L. J. Rosenberg, C. Hagmann, D. Kinion, W. Stoffel, K. van Bibber, P. Sikivie, N. S. Sullivan, D. B. Tanner, F. Nezhric, M. S. Turner, D. M. Moltz, J. Powell, M.-O. André, J. Clarke, M. Mück, and R. F. Bradley, *Phys. Rev. D* **64**, 092003 (2001).
- ⁷¹S. J. Asztalos, G. Carosi, C. Hagmann, D. Kinion, K. van Bibber, M. Hotz, L. J. Rosenberg, G. Rybka, J. Hoskins, J. Hwang, P. Sikivie, D. B. Tanner, R. Bradley, and J. Clarke, *Phys. Rev. Lett.* **104**, 041301 (2010).
- ⁷²D. Kinion, "First results from a multiple-microwave-cavity search for dark-matter axions," Ph.D. thesis, University of California Davis, 2001.
- ⁷³D. Alesini, C. Braggio, G. Carugno, N. Crescini, D. D'Agostino, D. Di Gioacchino, R. Di Vora, P. Falferi, S. Gallo, U. Gambardella, C. Gatti, G. Iannone, G. Lamanna, C. Ligi, A. Lombardi, R. Mezzena, A. Ortolan, R. Pengo, N. Pompeo, A. Rettaroli, G. Ruoso, E. Silva, C. C. Speake, L. Taffarello, and S. Tocci, *Phys. Rev. D* **99**, 101101 (2019).
- ⁷⁴K. M. Backes, D. A. Palken, S. A. Kenany, B. M. Brubaker, S. B. Cahn, A. Droster, G. C. Hilton, S. Ghosh, H. Jackson, S. K. Lamoreaux *et al.*, *Nature* **590**, 238–242 (2021).